



## RESEARCH ARTICLE

10.1029/2019JD030768

# The Dependence of Shallow Cumulus Macrophysical Properties on Large-Scale Meteorology as Observed in ASTER Imagery

Theresa Mieslinger<sup>1,2</sup> , Ákos Horváth<sup>1</sup> , Stefan A. Buehler<sup>1</sup> , and Mirjana Sakradzija<sup>3</sup> <sup>1</sup>Faculty of Mathematics, Informatics and Natural Sciences, Department of Earth Sciences, Meteorological Institute, Universität Hamburg, Hamburg, Germany, <sup>2</sup>International Max Planck Research School on Earth System Modelling, Hamburg, Germany, <sup>3</sup>Max Planck Institute for Meteorology, Hamburg, Germany**Key Points:**

- We investigate the sensitivity of shallow cumulus cloud fields to large-scale meteorology with high-resolution satellite imagery
- We identify surface wind speed as the dominant cloud-controlling factor in our data set
- We confirm the robust representation of cloud size distributions by a double power law

**Correspondence to:**T. Mieslinger,  
theresa.mieslinger@mpimet.mpg.de**Citation:**Mieslinger, T., Horváth, Á., Buehler, S. A., & Sakradzija, M. (2019). The dependence of shallow cumulus macrophysical properties on large-scale meteorology as observed in ASTER imagery. *Journal of Geophysical Research: Atmospheres*, 124, 11,477–11,505. <https://doi.org/10.1029/2019JD030768>

Received 5 APR 2019

Accepted 19 AUG 2019

Accepted article online 29 AUG 2019

Published online 8 NOV 2019

**Abstract** This study identifies meteorological variables that control the macrophysical properties of shallow cumulus cloud fields over the tropical ocean. We use 1,158 high-resolution Advanced Spaceborn Thermal Emission and Reflection Radiometer (ASTER) images to derive properties of shallow cumuli, such as their size distribution, cloud top heights, fractal dimensions, and spatial organization, as well as cloud amount. The large-scale meteorology is characterized by the lower-tropospheric stability, subsidence rate, sea surface temperature, total column water vapor, wind speed, wind shear, and Bowen ratio. The surface wind speed emerges as the most powerful control factor. With increasing wind speed the cloud amount and cloud top heights show a robust increase accompanied by a marked shift in the cloud size distribution toward larger clouds with smoother shapes. These results lend observational support to the deepening response of a wind-driven marine boundary layer as simulated by large-eddy models. The other control factors cause smaller changes in the cloud field properties. We find a robust increase in cloud amount with increasing stability and decreasing sea surface temperature, respectively, which confirms a well-known behavior of marine stratocumulus also for shallow cumulus clouds. Due to the high resolution of cloud images, we are able to study the lower end of the cloud size distribution and find a robust double power law behavior with a scale break at 590 m. We find a variation in the shape of the cloud size distribution with Bowen ratio, qualitatively consistent with modeling results and suggesting the Bowen ratio as a new potential control factor on shallow cumulus clouds.

## 1. Introduction

We identify large-scale meteorological drivers of shallow cumulus macrophysical properties from an extensive high-resolution observational data set. Previous literature demonstrates that data limitations impede the investigation of primary control factors on shallow cumulus or trade wind cumulus clouds within the tropical marine boundary layer, while at the same time, such clouds play a crucial role in the Earth's radiative balance. Due to their high-albedo and ubiquitous nature, they reflect a substantial amount of shortwave radiation and cool the Earth system. These low-level warm clouds have been identified as the main source of divergence in estimates of climate sensitivity, as their representation in global climate models, especially their coupling to the large-scale flow, is still problematic (Bony & Dufresne, 2005; Vial et al., 2018). Accurately modeling the sign and magnitude of low-cloud feedback in a warming climate does therefore require an understanding of how the large-scale meteorological conditions govern the microphysical and macrophysical properties of shallow cumulus clouds.

Mean subsiding motion and the resulting enhanced stability largely identify the areas where low-level clouds are prevalent. Well-established measures of environmental controls on low-level cloud fields are correspondingly the subsidence rate and the lower-tropospheric stability (LTS), which is the potential temperature difference between 700 hPa and the surface (Klein & Hartmann, 1993; Slingo, 1987). Wood and Bretherton (2006) show that LTS and variations thereof can be used to discriminate between stratocumulus and shallow cumulus cloud fields. Stratocumulus decks favor the cool sea surfaces of eastern boundary currents, which are associated with large LTS, a shallower boundary layer, a strong capping temperature inversion, and stronger subsidence. Shallow cumuli, on the other hand, tend to form over warm surfaces deeper in the tropics, which are characterized by smaller LTS, a deeper boundary layer, a weaker inversion, and

©2019. The Authors.

This is an open access article under the terms of the Creative Commons Attribution License, which permits use, distribution and reproduction in any medium, provided the original work is properly cited.

somewhat weaker subsidence. A threshold value of about 18.5 K can generally distinguish between the high-LTS stratocumulus and low-LTS shallow cumulus regimes (Klein & Hartmann, 1993; Medeiros & Stevens, 2011). These two basic cloud regimes are not sharply separated though but instead are connected through transition regions where stratocumulus begins to break up with shallow cumuli developing underneath (Sandu & Stevens, 2011). To our knowledge there is no study yet that investigates the potential of LTS on controlling different cloud field states within the shallow cumulus cloud regime and that goes beyond the bulk cloudiness.

In addition to LTS, several other factors controlling low clouds were identified in both observational and large-eddy simulation (LES) modeling studies; for a recent review see Klein et al. (2018). For example, subsiding motion and sea surface temperature (SST) often covary such that cold SSTs enhance subsidence and atmospheric stability, both leading to an increase in low-level cloudiness (Qu et al., 2015). Similarly, increased free-tropospheric humidity and increased horizontal cold air advection are both positively correlated with low-cloud amount (Myers & Norris, 2016; Norris & Iacobellis, 2005). We refer to the free troposphere as the layer above the planetary boundary or trade wind boundary layer, which includes the well-mixed subcloud layer and the cloud layer. Concerning the influence of humidity, Stevens et al. (2018) point to the regulating role of water vapor and its distribution in the tropical lower troposphere on cloud patterns. Furthermore, prevailing surface easterly winds are a prominent feature of subtropical regions over ocean, which are often called the trades or trade wind region. A recent study around Barbados revealed a high influence of surface wind speed on cloud cover (Brueck et al., 2015), while some modeling studies even claim that surface winds are a major control to shallow cumulus cloud fields in the trades (Nuijens & Stevens, 2012; Nuijens et al., 2015).

The properties of shallow cumulus clouds are reduced to cloud amount as the sole measure of tropical low-level cloudiness in most previous studies. The strong emphasis on cloud amount stems from the fact that it is one of the most relevant parameters to radiative flux and thus cloud feedback calculations, which current climate models struggle to properly simulate. Other cloud field properties, such as the size distribution and spatial organization of clouds, have received less attention, although the cloud size distribution in particular is a key parameter used in parameterization schemes to calculate the mass flux and energy transported within individual clouds (Neggers et al., 2003). Cloud size distributions are commonly described by a power law and its scaling parameter. The derivation of scaling parameters is handled rather inconsistently in the literature, leading to a wide range of published values. Furthermore, the spatial distribution or spatial clustering of clouds was found to influence the large-scale meteorological field. On the mesoscale, Tobin et al. (2012, 2013) observed clustered cloud fields in drier atmosphere and with reduced cloud amount. The latter heavily affects the outgoing longwave radiation and the vertical distribution of heating rates and may force large-scale circulation patterns. Whether such behavior extends down to small-scale shallow cumuli is an open question.

Previous literature demonstrates shortcomings in the investigation of the shallow cumulus regime due to coarse-resolution and small observational data sets. Past investigations had to rely on airborne observations, land surface-imaging satellite sensors, or ground-based measurements due to the coarse spatial resolution of most meteorological satellite imagers. In fact, there is no high-resolution space-borne imager dedicated to cloud observations in orbit today. Early studies used 30- to 60-m resolution Landsat images (Cahalan & Joseph, 1989; Gotoh & Fujii, 1998; Sengupta et al., 1990; Wielicki & Welch, 1986) or aerial photography (Benner et al., 1998; Plank, 1969) to estimate the cloud size distribution of shallow cumuli. Although these works clearly demonstrated the potential of high-resolution cloud imagery, they lacked statistical significance for only a handful of scenes were analyzed. The two most recent observational studies, on the other hand, principally relied upon ground-based radar, lidar, and ceilometer measurements at the Barbados Cloud Observatory (BCO), aided by Moderate-Resolution Imaging Spectroradiometer (MODIS) low-level cloud cover estimates derived from 1-km resolution pixel data (Brueck et al., 2015; Nuijens et al., 2015).

By far the most comprehensive and statistically robust satellite study of shallow cumulus is that of Zhao and Di Girolamo (2007), which analyzed 152 Advanced Spaceborne Thermal Emission and Reflection Radiometer (ASTER) scenes collected west from the Caribbean islands during the Rain in Cumulus over the Ocean (RICO) campaign. From the 15-m-resolution ASTER images, they derived statistics for the macro-physical properties of shallow cumulus cloud fields, including cloud fraction, cloud size, fractal dimension,

cloud top height (CTH), and cloud spatial horizontal distribution. However, this study did not find any relationship between the large-scale meteorology and any of the estimated cloud macrophysical properties. The authors hypothesized this was due to the inability of their forecast data to capture the large-scale meteorological conditions during RICO. It might also have been the case that even Zhao and Di Girolamo (2007)'s extended data set was too small to reveal dependencies on cloud-controlling parameters. Regardless, it bolsters the call made by the latest review of Klein et al. (2018) for further observational studies of shallow cumulus clouds.

The goal of our study is to take advantage of the public availability of the global ASTER data archive, expand upon the work of Zhao and Di Girolamo (2007), and identify the primary control factors of shallow cumulus cloud fields. We analyze 1,158 trade wind cumulus scenes drawn from the western Atlantic and the central and eastern Pacific, which constitute a data set about an order of magnitude larger than in any earlier work. We investigate the amount, size distribution, fractal dimension, top height, and spatial organization of shallow cumulus clouds as a function of large-scale meteorology characterized by ERA-Interim reanalysis. The considered cloud-controlling factors include LTS, subsidence rate, total column water vapor (TCWV), SST, surface wind speed, wind shear, and Bowen ratio. The Bowen ratio is the ratio of the surface sensible heat flux to the latent heat flux and has been proposed by a recent LES study of Sakradzija and Hohenegger (2017) to control the distribution of shallow cumulus cloud base mass flux and thus cloud size distribution.

The paper is organized as follows. Section 2 describes the ASTER images and reanalysis data set, the cloud masking algorithm, and the derivation of macrophysical cloud field properties. Section 3 then shows overview statistics of these cloud field properties, including information on the representation of cloud size distributions. Here, we also show that the considerable scatter in previously reported scaling parameters of power law cloud size distributions is to a large degree the result of inconsistent fitting and data binning strategies. Section 4 presents the variation in observed cloud field properties with large-scale meteorological parameters with a focus on the dominant control variable surface wind speed. Finally, section 5 summarizes our results.

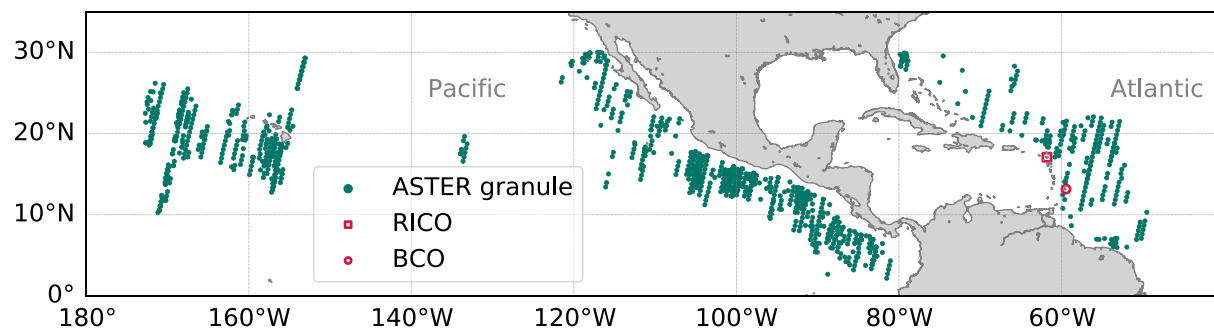
## 2. Data and Methods

### 2.1. ASTER Imagery

ASTER flies aboard Terra, a polar-orbiting satellite in a Sun-synchronous orbit with an equator crossing time of 10:30 local solar time. ASTER consists of one nadir and one backward-pointing camera. The nadir camera, whose imagery is used exclusively in this study, has three separate radiometers. The visible and near-infrared sensor covers the range from 0.53 to 0.86  $\mu\text{m}$  in three bands with 15-m spatial resolution. The radiometer in the shortwave infrared (SWIR) range consists of six bands in the range of 1.60–2.43  $\mu\text{m}$  at 30-m resolution, and the thermal infrared (TIR) radiometer comprises five bands covering 8.125–11.65  $\mu\text{m}$  with 90-m spatial resolution (Abrams et al., 2000; Yamaguchi et al., 1998). ASTER data are available in  $60 \times 60 \text{ km}^2$  scenes, each corresponding to 9 s of observation time.

The data set is limited by the opportunistic nature of data acquisition over the ocean. ASTER was designed for land surface studies and thus prioritizes cloud-free and land observations. Nevertheless, it has also acquired a large number of oceanic cloud scenes, often in support of atmospheric field campaigns such as RICO. It should be noted, however, that ASTER's sampling of clouds is rather irregular as a result. Starting in May 2007, the SWIR detector suffered temperature problems, leading to image striping and saturation effects. Therefore, we only consider data from 2000 to mid 2007, as the cloud masking algorithm described in section 2.2 relies on a SWIR band.

We filter the available images for pure shallow cumulus cloud fields in the tropics. The study area is limited to the Northern Hemisphere from  $0^\circ \text{ N}$  to  $30^\circ \text{ N}$ , zonally covering the central and eastern Pacific as well as the western Atlantic. Cloudy scenes dominated by stratocumulus, affected by sun glint, or contaminated by cirrus are eliminated. The latter turned out to be a major constraint, because many shallow cumulus scenes also show high-level cirrus clouds. The presence of cirrus clouds likely indicates additional dynamical influences to the meteorological state that would complicate our analysis. Such scenes are therefore excluded. Thin cirrus is often transparent in the visible bands but can easily be detected in ASTER's TIR bands from their cold cloud top temperatures. We find that 47 of the 152 scenes of Zhao and Di Girolamo (2007) have



**Figure 1.** The geographical location of the ASTER images of shallow cumulus cloud fields comprising our data set collected between 2000 and 2007. The 1,158 images are depicted by green circles, 325 of which are around Hawaii in the central Pacific, 613 in the eastern Pacific, and 220 in the western Atlantic. The location of the Rain in Cumulus over the Ocean (RICO) field campaign and that of the Barbados Cloud Observatory (BCO) are indicated with red shapes.

some cirrus contamination, although this did not have a major effect on their results as the authors relied on visually derived cloud masks based on a visible channel only. Our final data set, including the 105 cirrus-free scenes from Zhao and Di Girolamo (2007), consists of 1,158 carefully selected and visually checked ASTER scenes of tropical shallow cumulus, the geographic locations of which are plotted in Figure 1.

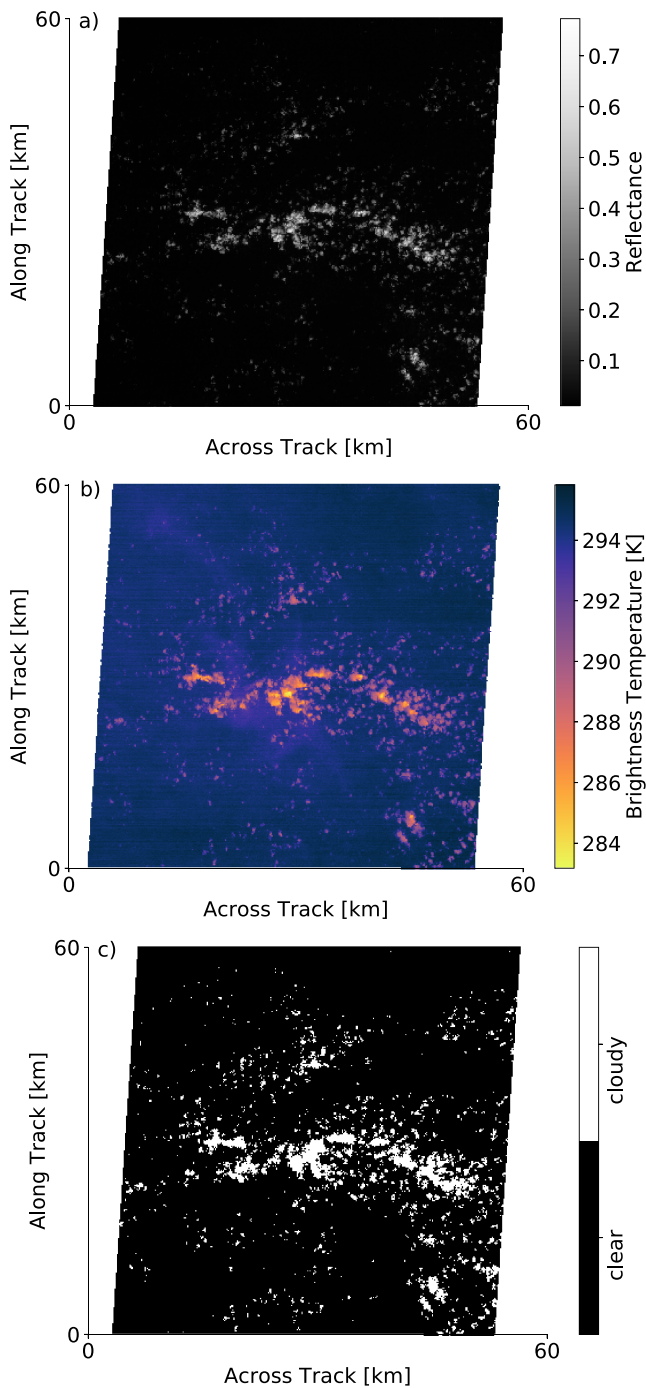
## 2.2. ASTER Cloud Mask and Cloud Object Labeling

ASTER does not have operational cloud products; thus, a cloud mask has to be derived independently. Previous high-resolution cloud studies were based on visually derived cloud masks using manually tuned thresholds, which are unfeasible for analyzing a large number of images (Benner et al., 1998; Cahalan & Joseph, 1989; Zhao & Di Girolamo, 2007).

Therefore, we implement the automated ASTER cloud masking technique of Werner et al. (2016) with the addition of a Sun glint filter. This algorithm employs five threshold tests, similar to the MODIS cloud detection scheme, and classifies each 15-m pixel as *clear*, *probably clear*, *probably cloudy*, or *cloudy*. Four tests are based on reflectivity thresholds in the visible and near-infrared and SWIR range and are designed to distinguish between bright clouds and the dark ocean. Under strong Sun glint or broken cloud conditions, an additional test based on band 14 (11.65  $\mu\text{m}$ ) is applied to correct warm ocean pixels that are labeled cloudy after the first four tests. In such cases, however, the effective resolution of the cloud mask is noticeably reduced to that of the coarser (90-m resolution) thermal channel. To avoid the degradation of the cloud mask, all images with possible Sun glint are excluded from our data set. First, the glint angle is computed for each pixel from the sensor-Sun geometry information stored in L1B file metadata (Yang et al., 2015). Then pixels with a glint angle below a threshold are flagged as potentially Sun glint contaminated. From visual inspection we find that a threshold value of 25° efficiently eliminates glint affected and thus reduced-resolution cloud masks. Finally, the *clear* and *probably clear*, as well as the *cloudy* and *probably cloudy* classes are merged to create a binary (*clear*, *cloudy*) mask, from which all subsequent cloud field properties are derived.

Figure 2 shows a typical ASTER shallow cumulus scene on 9 September 2004 over the Atlantic ocean. Reflectances from band 3 (0.86  $\mu\text{m}$ , nadir) in Panel (a) exemplify the information content from the visible bands used in reflectivity thresholding tests. Panel (b) shows a false-color image of brightness temperatures from ASTER's thermal band 14 (11.65  $\mu\text{m}$ ). High and cold cloud tops are clearly visible in yellowish colors. Three further channels contribute information to the final cloud mask shown in panel (c). We evaluate the performance of the automated cloud masking algorithm of Werner et al. (2016) against the manually constructed reference cloud masks described in Zhao and Di Girolamo (2007). From a direct comparison of 105 cirrus-free cloud images, we find that cloud field properties such as cloud fraction, cloud size distribution, and fractal dimension agree well with the work of Zhao and Di Girolamo (2007), confirming that the automated cloud masking scheme adequately detects marine shallow cumulus clouds.

Based on the binary cloud mask, individual cloud objects are defined with the four-connectivity rule, which groups neighboring cloudy pixels sharing an edge into the same cloud but treats cloudy pixels sharing only a



**Figure 2.** ASTER scene recorded on 9 September 2004 at 14:12:47 UTC showing (a) reflectances from the visible and near-infrared band 3 (0.86  $\mu\text{m}$ , nadir) in gray scale, (b) a false-color image of brightness temperatures from the thermal band 14 (11.65  $\mu\text{m}$ ), and (c) the cloud mask derived following Werner et al. (2016).

vertex as separate clouds. Single-pixel clouds are found to mostly reflect instrument noise and are therefore excluded from further calculations. The total number of clouds in the selected 1,158 ASTER images is 5,171,808.

### 2.3. Fractal Dimension

The geometric irregularity of shallow cumulus clouds can have important radiative impacts, as it has been found to significantly affect domain-averaged solar fluxes and atmospheric heating rate profiles (Hinkelman et al., 2007). The general complexity of cloud shapes can be characterized by the scaling relationship between cloud perimeter  $P$  and cloud area  $A$  (Lovejoy, 1982):

$$P \propto A^{\frac{d}{2}}, \quad (1)$$

where the exponent  $d$  is the fractal dimension. The fractal dimension is a statistical descriptor of inherent scaling, which does not uniquely define shapes. However, for regular shapes such as a circle,  $d$  is unity, while  $d$  would approach the value of two for increasingly fissured clouds with fractal perimeters, and equation (1) transforms to  $P \propto A$  accordingly.

We calculate the cloud area  $A$  from the sum of all pixels belonging to the same cloud entity and multiply it by the pixel area defined by the cloud mask resolution ( $15 \times 15 \text{ m}^2$ ). The cloud perimeter  $P$  can be defined in different ways; however, different definitions still produce a similar scaling relation (Cahalan & Joseph, 1989). In our study,  $P$  was calculated as the summed length of boundary line segments connecting the centers of cloud edge pixels. The fractal dimension  $d$  is then approximated from a linear least squares fit to a doubly logarithmic scatterplot of  $P$  versus  $A$ . For small clouds the slope is sensitive to the perimeter algorithm and the pixel shape. Because the pixel shape is regular, the derived fractal dimension tends to become smaller when more small clouds are included in the analysis and vice versa. However, we did not detect such artifacts in our analysis at small cloud sizes. In fact, we find the fractal dimension decreasing even when large cloud sizes are more abundant (see section 4).

### 2.4. Cloud Size Distribution

Shallow cumulus clouds exhibit sizes ranging over several orders of magnitude. The vast majority of clouds are small, and the cloud size distribution tails off toward less-frequent large clouds. As a result, empirical cloud size data are most commonly assumed to follow a power law distribution, both in observational and modeling studies. Whether this assumption is justified in a strict mathematical sense or the data are better described by other statistical distributions (lognormal, exponential, and stretched exponential) is an important topic in and of itself, which, however, is beyond the scope of this work. For an excellent review on the subject, the reader is referred to Clauset et al. (2009). Suffice it to say, one can hardly ever be certain that an observed quantity is truly drawn from a power law distribution due to the insufficient sampling of the distribution tail, which represents large but rare events. For consistency and compar-

ability with previous studies, we assume a power law distribution here but show that the most common method to estimate the scaling parameter, a least squares linear regression on data represented in a log-log plot, gives predictably different results depending on histogram binning scheme and the choice of cloud size measure.

If a quantity, such as the size of a cloud  $D$ , obeys a power law, it is drawn from a probability distribution:

$$n(D) \propto D^b, \quad (2)$$

where the (negative) exponent  $b$  is the *slope* or *scaling parameter*. The scaling parameter typically lies in the range of  $-3 < b < -2$  for natural phenomena.

Power laws were extensively used in the literature to characterize cloud size distributions. While early studies on shallow cumulus clouds found an exponential decrease in cloud number with increasing cloud size (Plank, 1969; Wielicki & Welch, 1986), or reported a lognormal behavior (López, 1977), more recent studies fit power laws to cloud size distributions (Benner et al., 1998; Cahalan & Joseph, 1989; Heus & Seifert, 2013; Koren et al., 2008; Neggers et al., 2003; Zhao & Di Girolamo, 2007). The scaling parameter is a characteristic measure of cloud size distributions, as it indicates the cloud sizes that contribute most to the cloud fraction. For example, a steep slope means the preponderance of small clouds. In the following, we explain in more detail the derivation of the scaling parameter for a power law and reveal some inconsistencies in the application of power law fits within the literature with the aim to make the various published numbers comparable.

The scaling parameter can be derived by taking the logarithm of both sides of equation (2) yielding the linear form

$$\log(n(D)) = \text{const.} + b \cdot \log(D). \quad (3)$$

In practice, the probability density function  $n(D)$  is estimated by constructing a histogram of the data. Then  $b$  is estimated as the slope of the least squares linear regression between the logarithm of the bin counts  $\log n(D)$  and that of the bin center values  $\log D$ . For cloud size distributions, one can either use a measure of length  $D$ , such as cloud area-equivalent diameter or the square root of the area  $\sqrt{A}$ , or alternatively the area  $A$ . Cloud area-equivalent diameter is a common length scale measure of cloud size, which we also use in this study. It is calculated from the cloud area by assuming a perfectly circular cloud.

The cloud size histogram can be constructed using bins of constant width, what we call *linear binning*, or bins of exponentially increasing width, referred to as *logarithmic binning*, where bins have the same width in logarithmic space. Note, however, that switching from  $D$  to  $A$  as the cloud size measure and switching from linear to logarithmic histogram binning both amount to a change of variable of the probability density function. Applying the well-known change-of-variable technique to transform the probability density function, it can be shown that if  $D$  follows a power law with exponent  $b$  as in equation (2), then

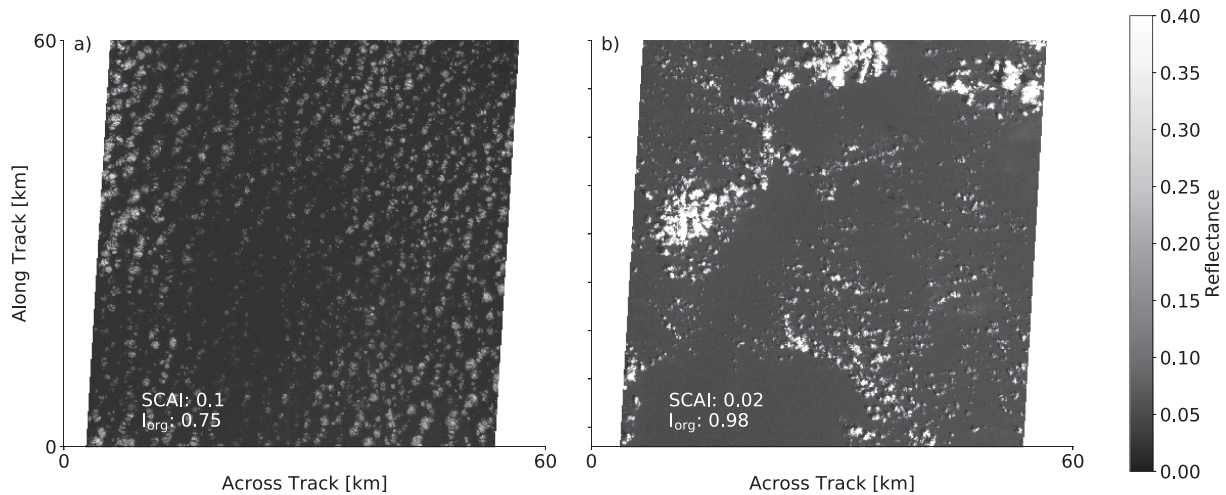
$$n(\log(D)) \propto D^{b+1}, \quad (4)$$

$$n(A) \propto A^{\frac{b-1}{2}}, \quad (5)$$

$$n(\log(A)) \propto A^{\frac{b+1}{2}}. \quad (6)$$

Using  $\sqrt{A}$  instead of  $D$  as length measure, on the other hand, yields a power law with the same exponent  $b$ , because  $\sqrt{A} \propto D$ . We provide an explicit derivation of  $n(\log D)$ ,  $n(A)$ , and  $n(\log(A))$  in Appendix A.

When displaying empirical data on a logarithmic scale, it is most appropriate to use bins that are equidistant in logarithmic space. Although many studies in the past used equal linear bin increments, we emphasize that displaying the data in such a way is misleading because the area below the curve does not represent the integral over the probability density as the reader might intuitively assume. Instead, the derivative  $dD/d(\log D)$  needs to be applied to  $n(D)$  for consistency (see equation (A3)). Using logarithmic binning is not only more adequate for the problem but it also allows the full range of cloud sizes to be taken into account for the derivation of the scaling parameter. In comparison, studies using linear bin increments, such as Benner et al. (1998) and Zhao and Di Girolamo (2007), only included cloud sizes up to 7 km or less to prevent the noisy upper part of the cloud size distribution from having a strong weight in the fitting procedure. From a sensitivity study (not shown), we conclude that the cloud size distribution changes strongly with bin size and fitted range of values when using linear binning, while the shape of the size distribution is more robust for logarithmic binning, confirming our argument in favor of logarithmic binning.



**Figure 3.** Example ASTER scenes showing reflectances from the visible and near-infrared band 3 ( $0.86 \mu\text{m}$ , nadir): (a) for an unclustered cloud field and (b) for a clustered cloud field. The corresponding Simple Convective Aggregation Index and  $I_{\text{org}}$  cluster indices are stated.

### 2.5. Cloud Spatial Distribution

In Figure 3 we show example ASTER images for different cloud spatial distributions: (a) randomly or regularly distributed clouds and (b) a clustered cloud field with arcs, cloud-free areas, and larger cloud objects. Assuming that in clustered shallow cumulus cloud fields small clouds merge and form larger cloud objects with cloud-free areas in between, the visual classification into unclustered and clustered states can be quantified by a combination of the number of clouds in a given domain and the distances between cloud objects. These two measures are combined differently in the two cluster indices, the Simple Convective Aggregation Index (SCAI) and the organization index  $I_{\text{org}}$ , which are commonly applied in cloud field studies.

#### 2.5.1. Simple Convective Aggregation Index

The SCAI was originally introduced by Tobin et al. (2012) for the description of deep convective clusters. It is a combination of two parameters, the number of clouds and the average distance between them, both of which are relevant in describing the clustering of points in an ensemble. For example, fewer clouds or shorter distances correspond to a higher degree of aggregation alike. The SCAI is calculated as the product of (i) the total number of clouds  $N$ , normalized by the maximum possible number  $N_{\text{max}}$  within a given domain, and (ii) a measure of the distance between the clouds  $l$ , normalized by the characteristic length scale of the domain  $L$ . That way the aggregation state is normalized by the maximum potential disaggregation.

The value of  $N_{\text{max}}$  is determined by the domain size, the pixel resolution, and the cloud labeling scheme. With the applied four-connectivity rule,  $N_{\text{max}}$  is half the number of pixels in a band 3N ASTER image. The characteristic cloud distance  $l$  is the geometric mean of all distances  $l_i$  between all possible cloud pairs, while  $L$  is set to the length of the diagonal of the  $60 \text{ km} \times 60 \text{ km}$  ASTER domain. The SCAI index is then calculated for each ASTER scene, expressed in per thousand, according to the following equation:

$$SCAI = \frac{N}{N_{\text{max}}} \frac{l}{L} \cdot 1,000, \quad (7)$$

where  $l = \sqrt[n]{\prod_{i=1}^n l_i}$  and  $n = N \cdot \frac{N-1}{2}$  is the number of cloud pairs.

One consequence of this definition is that SCAI can increase with  $N$  and independently also with  $l$ . However, these parameters are correlated and cannot vary completely independently in a fixed-size domain. A larger number of clouds in an ASTER image would alone lead to a higher SCAI, but SCAI might remain unchanged or even decrease due to a simultaneously decreasing distance between the clouds. However, Tobin et al. (2012) show that the value of  $N$  is dominating the value of SCAI. Similarly, we find  $N$  and SCAI highly correlated in our data set (Pearson correlation coefficient  $r=0.97$ ). Thus, low SCAI values can be related to aggregated cloud fields and high SCAI values to disaggregated situations.

A caveat to note is that the general magnitude of SCAI strongly depends on domain and pixel size, which makes the intercomparison of values derived from imagery of differing resolutions problematic. For example, the SCAI derived by Tobin et al. (2012) for  $10^\circ \times 10^\circ$  domains using 50-km-resolution brightness temperature data varies from 0 to 30, while in our ASTER data set the SCAI range is 2 orders of magnitude smaller. We therefore focus on relative changes in SCAI in section 4 without a direct interpretation of its absolute value.

### 2.5.2. Organization Index $I_{org}$

The second index used in our study is the organization index  $I_{org}$ , first introduced by Weger et al. (1992) and revisited by Tompkins and Semie (2017), which classifies a cloud field as regular, random, or clustered based on nearest neighbor (NN) distance statistics. If NN distances are on average smaller than expected from a random distribution, the cloud field is considered clustered; otherwise, it is deemed regular. Unlike the SCAI, the  $I_{org}$  is unambiguous to interpret due to the way it is constructed and can be compared among different sensors as it always ranges from zero to one. If shallow convection is randomly distributed and hence can be described by a Poisson point process, then the cumulative density function of nearest neighbor distances (NNCDF) exhibits a Weibull distribution of the following form:

$$NNCDF = 1 - \exp(-\lambda \pi l_n^2), \quad (8)$$

where  $\lambda$  is the average sample number per unit area and  $l_n$  is the single NN distances. In Figure 4e the theoretical Poisson NNCDF is plotted against the actual observed NNCDF. The  $I_{org}$  is the integral of the resulting curve (brown line). If the observed distribution of clouds is random, the curve will lie on the diagonal and  $I_{org} = 0.5$ . When the paired NNCDF curve is above the diagonal and  $I_{org} > 0.5$ , the cloud field is clustered. In contrast, when the curve is below the diagonal, the  $I_{org}$  is smaller than 0.5, and the cloud field has regular or random organization.

## 2.6. Cloud Top Height

CTH was derived at 90-m resolution from band 14 infrared window brightness temperatures, using the constant lapse rate method implemented in MODIS Collection 6 for marine stratocumulus under low-level inversion (Baum et al., 2012). The CTH is calculated from the difference in the brightness temperatures of cloudy and clear pixels observed at  $11 \mu\text{m}$  and divided by the season- and latitude-dependent apparent lapse rate taken from a lookup table published in Baum et al. (2012). Band 14 at  $11 \mu\text{m}$  is best suited for the retrieval because the water vapor absorption is low. Partial cloud cover can introduce a height bias as the assumed cloud emissivity of  $\epsilon = 1$  is a valid approximation only for fully cloudy pixels. To minimize such biases, we only derive CTH values for those 90-m pixels that are labeled fully cloudy by the 15-m-resolution cloud mask. Similarly, a 90-m pixel was only assumed clear if all its 15-m subpixels were labeled clear.

## 2.7. ERA-Interim Reanalysis and MODIS Data

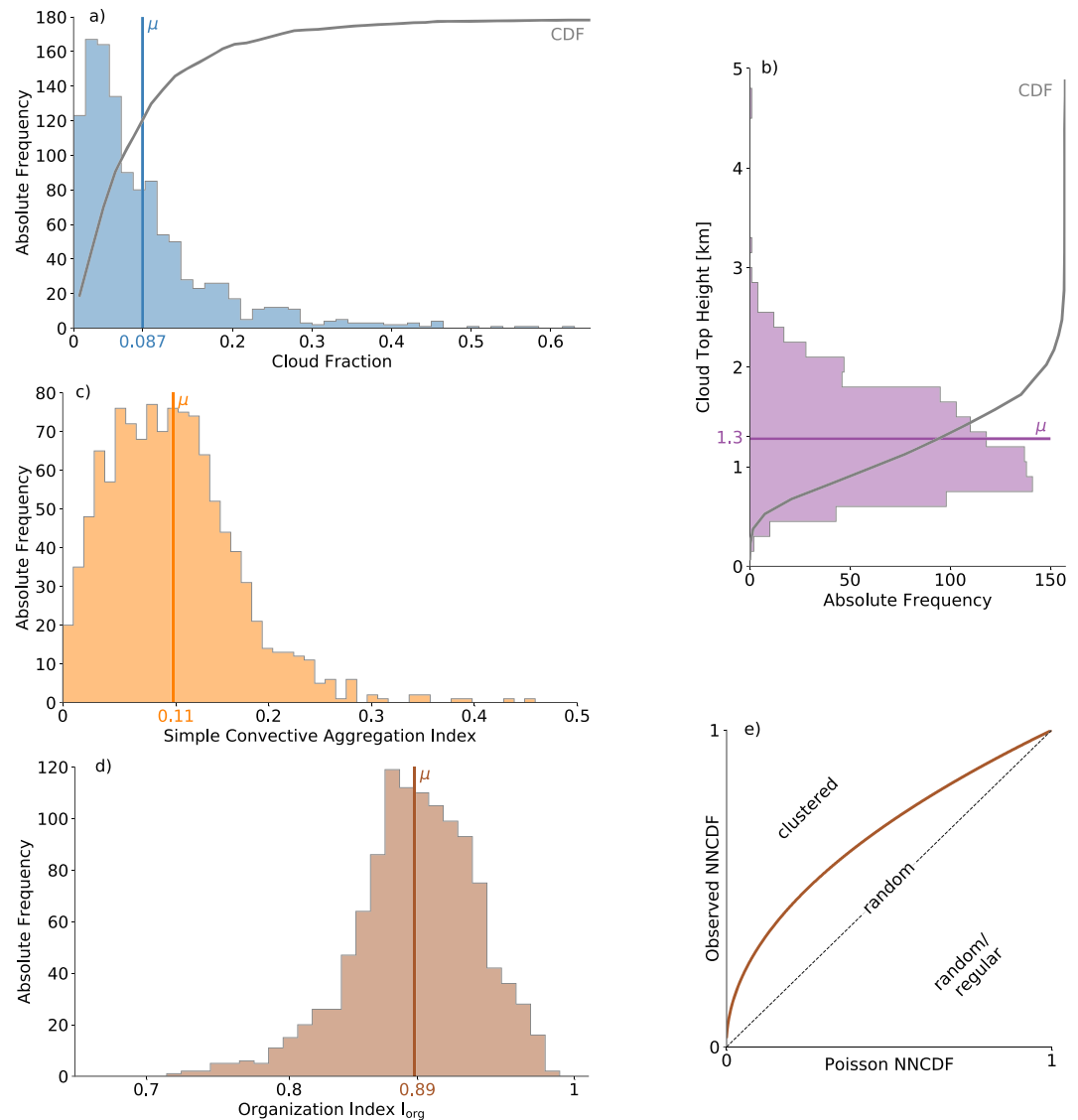
The large-scale meteorology is characterized on a per scene basis mostly by ERA-Interim reanalysis data, at a horizontal resolution of  $0.75^\circ$  or about 80 km (Berrisford et al., 2011; Dee et al., 2011). Meteorological variables from ERA-Interim are available every 6 hours, leading to a maximum time difference of 3 hours relative to the ASTER observations. We use the following single-level parameters: SST, surface wind speed at 10 m height, vertical velocity at the 700-hPa pressure level, and the Bowen ratio calculated from surface moisture and heat fluxes. The LTS and bulk wind shear in the boundary layer are derived from potential temperature and wind data between 1,000 and 700 hPa.

Scene-average TCWV is determined from ERA-Interim data and also from 5-km-resolution MODIS-Terra TIR retrievals (Collection 6 MOD05 product), which have perfect spatial and temporal coincidence with the ASTER scene. The TIR retrieval is favored here over the near-infrared retrieval product, because the latter does not provide values for thin and broken clouds (King et al., 2003). TCWV values from ERA-Interim and MODIS retrievals are found to be in very good overall agreement; thus, we only show results for the MODIS retrievals.

## 2.8. Analysis Method

The sensitivity of low clouds to large-scale meteorological fields is usually investigated by multiple linear regression (MLR) between a time series of detrended anomalies of cloud fraction (predictand) and that of selected meteorological parameters (predictors). Applying MLR to our data set would face various





**Figure 4.** Macrophysical properties of shallow cumulus cloud fields observed in 1,158 ASTER images. Panel (a) shows the frequency of cloud fraction, and Panel (b) the vertical distribution of scene-average cloud top heights.  $\mu$  gives the distribution average, while the gray line displays the cumulative density function (CDF). The clustering of clouds is shown in Panels (c) and (d) in terms of the Simple Convective Aggregation Index and organization index  $I_{org}$ . The sketch in Panel (e) illustrates the derivation of  $I_{org}$  from the CDF of nearest neighbor distances (NNCDF).

challenges though. First, ASTER's temporal sampling of clouds is highly irregular and episodic, preventing the creation of a continuous time series. Second, while MLR is well suited to model the variations in a simple quantity such as cloud fraction, its applicability is less obvious when analyzing the subtler properties of the cloud size distribution, such as power law exponent, scale break size, and spatial organization, which is the main focus of our paper. This is especially so, because the cloud size distribution cannot be accurately determined from a single scene. A number of scenes have to be aggregated to obtain reasonable estimates of distribution parameters, which unavoidably causes some convolution of the underlying meteorological parameters. Third, the minimum required sample size for MLR, which is a strong function of the squared multiple correlation coefficient, the desired accuracy of the prediction model, and the number of predictor variables, can easily exceed the size of our current ASTER data set (Knofczynski & Mundfrom, 2008).

These limitations led us to adopt a simple approach, which characterizes the average cloud field properties as a function of a single binned meteorological control parameter at a time. The data subsets in each bin are

chosen such that they include a minimum amount of images, but not necessarily the same amount. Choosing the subsets strictly such that an equal amount of values is included does not change our results in a qualitative way. This approach cannot account for the interdependency between the various control parameters, and hence, the derived sensitivities are likely biased. Nevertheless, the dominant effect of a given meteorological parameter can still be teased out, at least in a qualitative sense. As we show in the following, well-established stratocumulus-meteorology relationships, for example, the increase in cloud fraction with increasing LTS and decreasing SST, are also reproduced in our shallow cumulus data, which lend confidence in the results.

### 3. Statistical Overview of Cloud Field Properties

#### 3.1. Cloud Fraction, CTH, Cloud Spatial Distribution, and Fractal Dimension

Based on the introduced cloud mask, the cloud amount in individual ASTER images ranges from 0% to about 60% with an average of 8.7%. The histogram and cumulative histogram of cloud fraction are shown in Figure 4a. Small values are dominating with a histogram mode between 1.5% and 4.5%, and about 90% of the images have a cloud fraction less than 20%. Although not by design, our average cloud fraction agrees very well with the average cloud fraction of 8.6% from Zhao and Di Girolamo (2007), indicating that the two data sets sample similar scenes of shallow cumuli.

Earlier studies report similarly low cloud fractions, one of the closest being a study by Benner et al. (1998) that reports an average cloud fraction of 9%. Observational studies reporting higher cloud fraction for shallow cumulus cloud fields often include cases at the transition to stratocumulus decks, which dominate the eastern coasts of the continents or deeper convective clouds in the proximity of the ITCZ (Brueck et al., 2015; Cahalan & Joseph, 1989). The calculated average cloud fraction is also far lower compared to ground-based measurements at the BCO, which can be viewed as a reference site for the trades. Nuijens et al. (2014) report an average cloud fraction of 30% from ceilometer measurements, about two thirds of which are contributed by low-level clouds at the height of the lifting condensation level. However, the ASTER images in our data set do not include stratiform cloud layers and large cloud systems, which are present at the BCO at certain times. Therefore, the observed low cloud fraction from ASTER images is reasonable, as only shallow cumulus clouds under suppressed conditions are included. The BCO measurements show that our ASTER scenes are not representative of the climatology of the whole trade wind region but rather correspond to a conditionally sampled (e.g., cirrus-free) subset.

Scene-average CTHs are found to be mostly below 3 km with a broad peak in the frequency distribution below the average CTH of 1.3 km (see Figure 4b). The studies of Zhao and Di Girolamo (2007) and Genkova et al. (2007) derived CTH values from ASTER imagery during the RICO campaign and found a bimodal frequency distribution with a primary peak at 0.9 km and a much smaller secondary peak at 1.5 km. Compared to such a double peak, we find one broad peak in a similar height level, which might be due to retrieval errors in the different CTH calculations mentioned. In general, several factors add uncertainty to the CTH retrieval. Zhao and Di Girolamo (2007) derive a high bias of about 200 m due to possible water vapor absorption above the cloud tops. On the other hand, Genkova et al. (2007) show that the ASTER infrared-window retrieval exhibits a low height bias of about 250 m on average compared to the more accurate stereo height retrieval, although the difference might have been caused by inadequate cloud motion correction in the stereo retrievals. In broken low-level cloud scenes, Greenwald et al. (2018) found a 450-m low bias in MODIS Collection 6 CTHs compared to Cloud-Aerosol Lidar with Orthogonal Polarization layer top heights, which was attributed to the influence of the warm ocean surface on 1-km MODIS brightness temperatures in partly cloudy pixels. This potential warm surface effect, however, is likely to be much smaller in the 90-m ASTER brightness temperatures. Based on the above, we estimate an overall minimum uncertainty of 300 m in our instantaneous pixel-level ASTER CTHs.

Analyzing the clustering indices SCAI and  $I_{org}$ , we find that both indices vary in a narrow range, between 0.0 and 0.6 with a mean of 0.1 for SCAI and between 0.7 and 1.0 with a mean of 0.9 for  $I_{org}$  (see Figures 4c and 4d). Both distributions are skewed toward aggregated or clustered states, SCAI showing a positive skewness and  $I_{org}$  showing a negative skewness. The quantitative interpretation of SCAI is generally very difficult. For reference, one-pixel clouds distributed in a checkerboard pattern would correspond to  $SCAI = 0.25$ . Therefore, most of the observed cloud fields in ASTER images are more clustered than such a

checkerboard pattern. The  $I_{org}$  on the other hand is a well-defined measure, which however classifies all cloud fields to be highly clustered. The narrow value range for both indices denotes a possible limited information content. In section 4 we therefore give only conservative interpretations of the changes in SCAI and  $I_{org}$  with meteorological variables.

We derive an overall fractal dimension of  $d=1.19$  from the full data set. The relatively small value implies that trade wind cumuli detected in our ASTER data set are rather compact and have smoother shapes compared to former studies (see Table 1). The fractal dimension derived in the present study significantly differs from the percolation theory value of  $d=1.33$ . Percolation can be viewed as a purely geometric null model for spatial clustering and also the related statistical properties, such as cloud sizes and their fractal dimension. A deviation from the percolation value indicates important physical or dynamical influences on the area-perimeter relation beyond pure geometric constraints (Peters et al., 2009).

### 3.2. A Critical View of the Power Law Fitting of Cloud Size Distributions

#### 3.2.1. ASTER Cloud Size Distribution

In Figure 5a the normalized cloud size distribution of all clouds detected in the ASTER data set is displayed in terms of the cloud area-equivalent diameter in black steps showing  $n(\log(D))$  (logarithmic binning) and in gray steps showing the deceptive  $n(D)$  (linear binning). The distribution follows two straight lines, which can be represented by a double power law with slopes for the small and the large cloud sizes, respectively. The threshold cloud size, the so-called scale break size  $D_c$ , is defined such that the two least squares fits result in the smallest combined error, which is, the sum of the squared residuals of both fits. In the present study, a separation at  $D_c=590$  m in the size distribution is found with the corresponding slopes of  $b_{log,1}=-0.68$  for  $D<D_c$  and  $b_{log,2}=-2.12$  for  $D>D_c$ . For consistency with previous literature, we also derive the scaling parameter for a single power law, leading to  $b_{log}=-1.55$ . For clarity, we explicitly label the scaling parameter as  $b_{log}$ , which is equivalent to  $b_{log}=b_{lin}+1$  according to equation (4).

Figure 5b shows the cloud area  $A$  distribution for logarithmic (black) and linear binning (gray). In the linear case, a fit is only performed up to  $A = 38 \text{ km}^2$ , which corresponds to  $D = 7 \text{ km}$ . The steps and linear regression fit for  $n(\log(A))$  mimic the fit for  $n(\log(D))$ , as there is a factor of 2 difference between the exponents, but the displayed range of  $A$  also covers double the orders of magnitude compared to the range of  $D$  values.

#### 3.2.2. On the Scale Break Size

We find a robust scale break in the cloud size distribution at  $D_c = 590$  m, similar to many past studies on shallow cumulus clouds that also apply a double power law. However, a physical interpretation of the scale break is by no means trivial and potential mechanisms controlling the scale break have been widely discussed. Peters et al. (2009) find that cluster properties, such as the size distribution, change with column water vapor in mesoscale convective systems. The authors hypothesize that former studies find different functional forms of the size distribution because they mix several atmospheric states characterized by differing water vapor contents. Based on percolation theory, they show that for certain column water vapor values, the size distribution exhibits a scale-free behavior without a break. A close match of the observed distribution slope with that from percolation theory would imply that the observed cloud fields are rich in scales. However, if simple percolation were the dominating factor, it would also imply that little could be learned from statistical parameters describing cloud fields, because such parameters are mainly the result of geometric constraints rather than any physical processes. A scale-free behavior would be in contrast to many studies arguing for the existence of a scale break size. Stevens (2005) even claims the scale break to be a controlling parameter of the size distribution of shallow cumulus clouds.

An argument supporting the scale break theory states that the natural horizontal scale of eddies within the boundary layer is directly linked to the vertical one. Plank (1969) finds a cloud width-to-height aspect ratio of about unity, meaning that one would expect clouds to exhibit a typical horizontal size of about the depth of the boundary layer, 500–700 m, which is close to the scale break size found in Figure 5 and within the range of values stated in the literature (see Table 1). In line with that, Cahalan and Joseph (1989) relate the scale break to the largest possible cluster size depicted by a single peak in reflectivity at cloud top compared to multiple peaks indicating a single cell being aggregated to clusters of cells with various reflectivity peaks resulting in a different scaling behavior of larger clouds. On the other hand, there is also criticism of the various existing scale break theories. Heus and Seifert (2013) show that poor sampling of large clouds in modeling studies produces a change in the slope of the size distribution. In sum, the existence of a true scale

**Table 1**  
Review of Cloud Size Distributions (Scaling Parameters and Scale Break Size), Fractal Dimensions, and Cloud Fractions of Shallow Cumulus Cloud Fields (sh.Cu.) From Different Observational (o) and Modelling (m) Studies and From Percolation Theory (t)

Study	Data type	No. of scenes (sh.Cu.)	n(x)	b	b <sub>1</sub>	b <sub>2</sub>	Scale break D <sub>c</sub> (km)	Fractal dimension d <sub>1</sub>	Fractal dimension d <sub>2</sub>	Cloud Fraction
Cahalan and Joseph (1989)	o	<17	logD	—	-1.6 (-0.6)	-3.3 (-2.3)	0.5	1.34	1.55	0.55
Sengupta et al. (1990)	o	10	D	—	-1.39 to -2.35	approximately -2 to -4	~1	1.20-1.27	1.5-1.73	—
Benner et al. (1998)	o	17	D	—	-1.98	-3.06	0.9	1.23	1.37	0.0925
Zhao and Di Girolamo (2007)	o	152	D	-2.85	-1.88	-3.18	0.6	1.28	—	0.086
Koren et al. (2008)	o	5	logA	-3.6 (-1.3)	—	—	—	—	—	0.1-0.25
Peters et al. (2009)	t/o	—	A	-3.12 (-2.06)	—	—	—	—	—	—
Neggers et al. (2003)	m	1 <sup>a</sup>	logD	—	-1.70 (-0.7)	—	0.7 <sup>a</sup>	—	—	0.14 <sup>a</sup>
Heus and Seifert (2013)	m	1	D	—	—	-2.2	0.4	—	—	0.138
Dawe and Austin (2012)	m	1	D	—	-1.88	—	1	—	—	—
Jiang et al. (2008)	m	1	D	—	-1.9 <sup>b</sup>	—	0.8	—	—	—
This study	o	1,158	logD	-2.55	-1.68	-3.12	0.59	1.19	—	0.087

Note. The scaling parameters  $b$ ,  $b_1$ , and  $b_2$  refer to the slope of a single power law and the slopes of a double power law, respectively, all according to equation (2). If slopes for  $n(\log D)$ ,  $n(A)$ , or  $n(\log A)$  are reported in a given study, those numbers are converted to  $b$  following equations (4), (5), or (6), and the original values is given in parenthesis. Fractal dimensions according to equation (1) are given, either assuming a double power law with the fractal dimensions  $d_1$  below and  $d_2$  above the scale break  $D_c$  or a single power law with the fractal dimension  $d_1$ .

<sup>a</sup>Large-eddy simulation results of Barbados Oceanographic and Meteorological Experiment (BOMEX) case only. <sup>b</sup>Cloud sizes range from 0.3 to 0.8 km.

break is still a matter of ongoing research, but our results show a scale break size that is close to the depth of the boundary layer.

### 3.2.3. On the Large Variation of Published Scaling Parameters

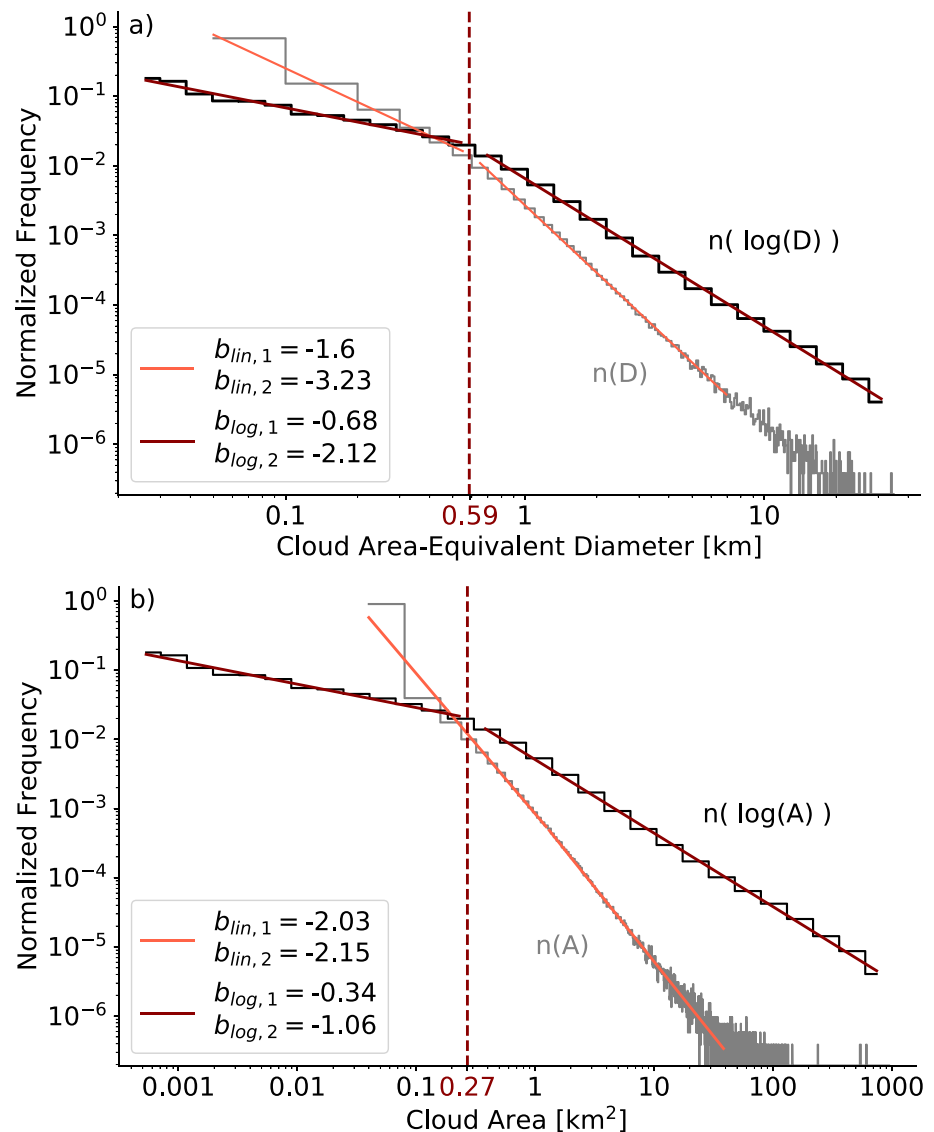
The different fitting procedures mentioned above can contribute to the inconsistency among published scaling parameters. In Table 1 we summarize scaling parameters of cloud size distributions from past observational and modeling studies and compare them to our results. Beyond listing the original values, we also attempt a first-order harmonization of the scaling parameters. Based on the choice of cloud size measure and binning scheme and using equations (2), (4), (5), and (6), the published exponents were converted to the equivalent exponent  $b_{lin}$  of a common reference corresponding to a power law in  $D$  and linear binning (see section 2.4). For example, we used logarithmic binning of  $D$  in our study; therefore, the slope resulting from a least squares linear regression  $b_{log}$  can be converted to  $b_{lin}$  by subtracting 1. These first-order corrections lead to better consistency among the scaling factors. Note, however, that there might be additional hard-to-estimate and hence uncorrected biases between published slopes, which arise from differences in sample size, bin width, or lower/upper cutoffs applied to the data. In a first attempt to harmonize the values, we assigned reported scaling parameters to either  $b$  or  $b_1$  and/or  $b_2$  depending on the range of cloud sizes used for the derivation and the assumption of a single or double power law. For example, Neggers et al. (2003) only derive one scaling parameter  $b_1$  up to a cutoff at the scale break size  $D_c$  and argue that no clear behavior can be found for larger cloud sizes. We believe that different scaling parameters in the literature are partly a result of differing fitting strategies and most likely also of too small data sets. We note that in some previous studies, scaling parameters derived by different fitting strategies were directly and thus erroneously compared.

Besides the inconsistency in fitting strategies, the identification of a power law distribution of cloud sizes by a straight-line behavior in a log-log plot can also be questioned. Clauset et al. (2009) states that “such straight-line behavior is a necessary but by no means sufficient condition for true power law behavior” from a statistical point of view. The most important shortfalls are the poor representation of the distribution tail and the sensitivity of slope estimates to the choice of the bin width. As an alternative, Clauset et al. (2009) proposed a potentially more accurate maximum likelihood estimator (MLE), which is calculated solely from the observed cloud diameter without binning. For the ASTER data we derived two exponents with the MLE method. For small clouds with  $D < D_c$  we find  $b_{MLE,1} = -1.9$ , and for large clouds with  $D > D_c$  we calculate  $b_{MLE,2} = -3.1$ . Both MLE scaling parameters are close to the corresponding values derived by linear regression on logarithmic binned cloud area-equivalent diameters  $D$ , confirming that the latter method also results in reasonable values for our data set. Based on the above, we use the double power law with its scaling parameters and the scale break size to characterize cloud size distributions in the following analysis.

## 4. Relations of Cloud Field Properties to Large-Scale Meteorological Parameters

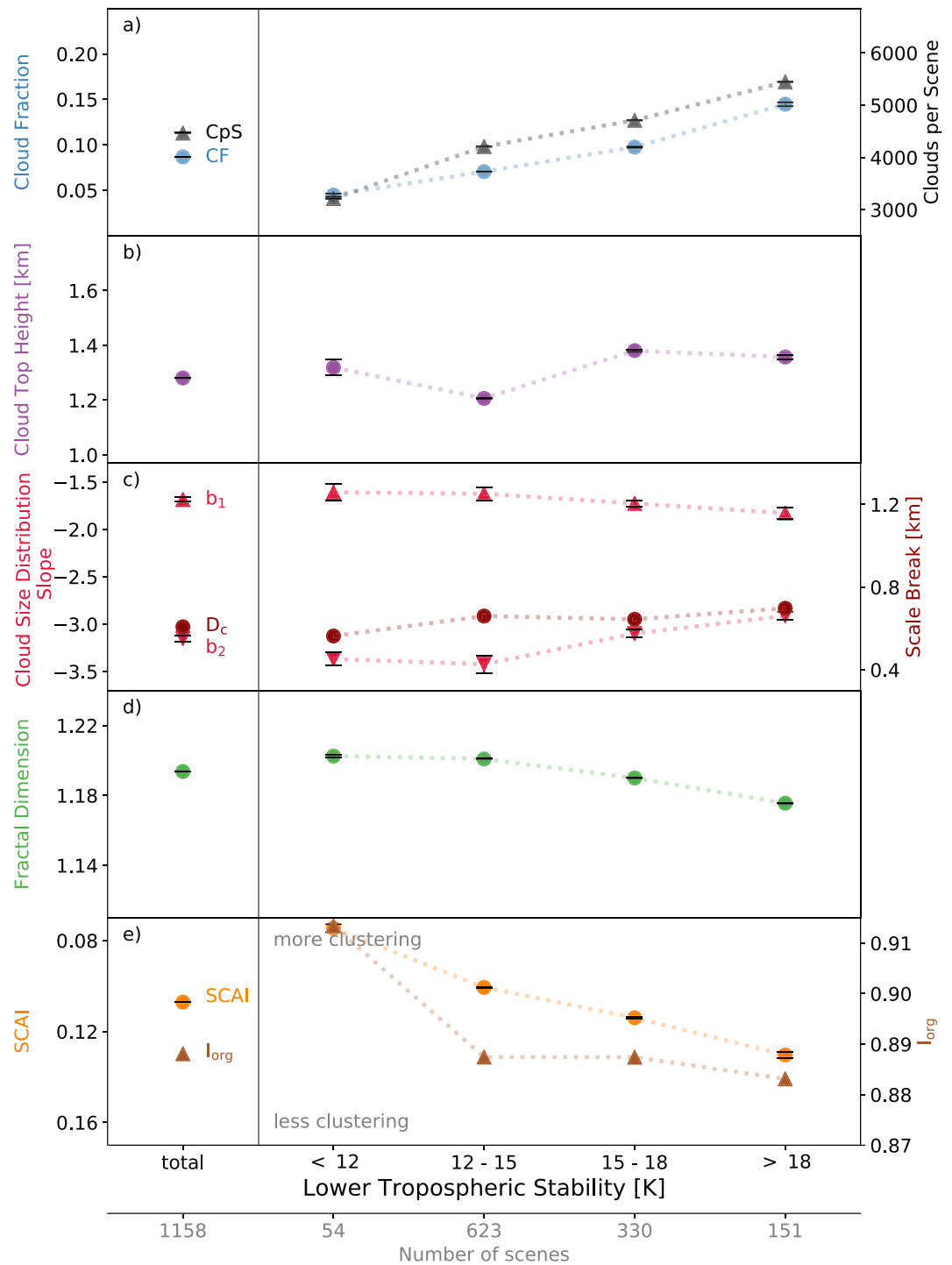
### 4.1. LTS and Subsidence

During the dry winter season, the trades are dominated by subsiding air masses and shallow cumulus, while deeper clouds are found during summer months under weak rising motion (Brueck et al., 2015). The sampled ASTER



**Figure 5.** Cloud size distribution of clouds detected in 1,158 ASTER images. (a) The distribution of cloud area-equivalent diameter ( $D$ ); (b) the corresponding cloud area ( $A$ ) covering the same range of cloud sizes. Gray steps and light red lines depict the size distribution and double power law fit using *linear binning* with equally sized 100-m bins for ( $D$ ) and 7,854 m<sup>2</sup> bins for cloud area ( $A$ ) with the scaling parameters  $b_{lin}$ . The black steps and the dark red lines show the data and the double power law fit with scaling parameters  $b_{log}$  for *logarithmic binning*. In that latter case, the frequency given on the y axis is  $n(\log(D))$  and  $n(\log(A))$  correspondingly. The scale break size  $D_c$  (dark red dashed line) is located where the double power law fit results in a minimum combined least squares error in the logarithmic case. Note that the area under the curve is only meaningful for the logarithmic case.

images cover a large variety of conditions ranging from weak rising to moderate subsiding motion. The subsidence strength is positively correlated with the LTS (Brueck et al., 2015; Myers & Norris, 2013), which is the potential temperature difference between 700 hPa and the surface. LTS is a well-established thermodynamic control on tropical low clouds, which has been used in the parameterization of marine stratiform cloud cover in general circulation models (Rasch & Kristjansson, 1998; Slingo, 1987). The LTS is essentially a bulk measure of the strength of the capping inversion. A stronger inversion, that is, higher LTS, reduces entrainment drying and warming, permitting a moister marine boundary layer and greater cloud cover (Myers & Norris, 2013; Wood & Bretherton, 2006). In Figure 6 we show variations in cloud field properties with increasing LTS. The vast majority of our scenes have a moderate LTS < 18.5 K, which was the threshold value



**Figure 6.** Cloud field properties as a function of lower-tropospheric stability. The properties derived from 1,158 ASTER images are sorted according to the scene-average lower-tropospheric stability calculated from ERA-Interim reanalysis temperatures. (a) Cloud fraction and (b) the cloud top height. In (c), the size distribution of cloud area-equivalent diameters is represented by the scaling parameters  $b_1$  and  $b_2$  of a double power law fit with the scale break size  $D_c$ . The fractal dimension  $d$  is plotted in (d), while the spatial distribution of clouds is quantified by the cluster indices Simple Convective Aggregation Index (SCAI; note that y axis is reversed) and  $I_{org}$  in (e). Error bars display the standard error in the mean for average values and the error in the slope for the scaling parameters and fractal dimension.

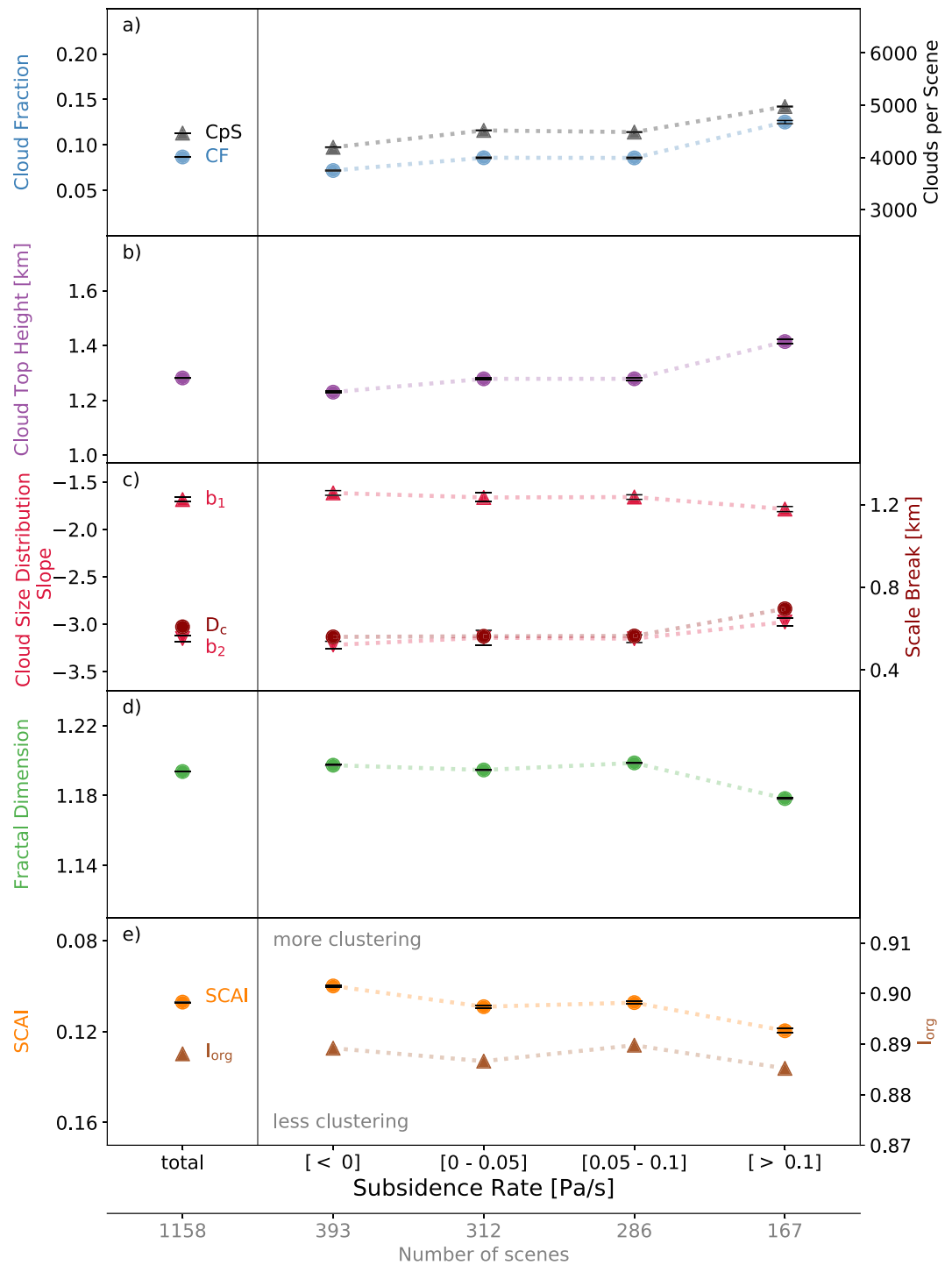


Figure 7. Same as Figure 6, but for subsidence rate at the 700-hPa pressure level.

used by Medeiros and Stevens (2011) to discriminate between shallow cumulus and stratocumulus in general circulation model simulations.

The cloud fraction increases from 5% to 15% with increasing stability. However, the rate of increase is only 3%/K, which is smaller than the sensitivities observed for stratocumulus. Klein and Hartmann (1993) derived a cloud fraction increase with LTS of 6%/K, Myers and Norris (2013) estimated a cloud fraction

sensitivity to the LTS related Estimated Inversion Strength (EIS) of 3.5–5.8%/K, and Qu et al. (2015) found EIS slopes in the range 1.7–3.5%/K. Consistent with LTS, cloud fraction also increases with increasing subsidence, where subsidence is expressed by the pressure vertical velocity at 700 hPa (Figure 7). However, the signal is much weaker compared to LTS. Subsidence seems to set the general conditions for the development of trade wind cumuli, but cloud field properties remain fairly constant for subsidence rates smaller than 0.1 Pa/s, which agrees with findings of Eitzen et al. (2011) for marine stratocumulus.

In contrast to the increase in cloud fraction, CTH stays fairly constant with increasing subsidence and stability. However, the change in cloud cover partly results from the change in cloud size distribution. We observe a change to steeper (more negative)  $b_1$  slopes, considerably less steep  $b_2$  slopes, accompanied by a slight increase in the scale break size from 0.55 to 0.70 km. All parameters indicate a relative shift of the cloud size distribution toward more frequent large clouds, which is accompanied by an overall increase in the total number of clouds detected. We hypothesize that in situations of strong subsidence and high-LTS clouds spread laterally at a strong inversion layer. Therefore, individual projected cloud areas, as well as the overall cloud fraction, increase. Our results are in line with observations at the BCO, where LTS was identified to control low-cloud amount (Brueck et al., 2015).

The fractal dimension shows only a marginal decrease meaning that cloud shapes do not change significantly. In general, the fractal dimension tends to approach smaller values (smoother shapes), whenever the scaling parameters of the cloud size distribution indicate larger clouds in our data set. However, dependencies of fractal dimension on certain meteorological parameters are usually small. The last panel in Figure 6 provides insight into the change in the spatial clustering of observed cloud fields. Both applied indices, SCAI and  $I_{org}$ , show a decrease in spatial aggregation with increasing stability. Note that disaggregated states correspond to high SCAI and low  $I_{org}$  values. High LTS, often related to strong subsidence, seems to inhibit clouds from organizing into clusters or arcs, which can frequently be seen over tropical oceans. However, we note that both indices have major shortcomings as discussed in section 2.5 and results should not be overinterpreted.

Myers and Norris (2013) argue that the climatological positive correlation between subsidence and marine boundary layer cloudiness is not the result of a direct physical mechanism but rather arises because enhanced subsidence is usually associated with larger LTS (stronger temperature inversion), which promotes greater cloudiness. They point out that enhanced subsidence alone actually leads to reduced cloud fraction by lowering the top of the boundary layer. The independent effect of enhanced subsidence and the associated effect arising from its covariation with LTS are therefore opposite, which can lead to partial cancelation. This might explain the insensitivity of cloud properties to subsidence in our bin analysis, which cannot separate out these two opposing mechanisms. The increase in shallow cumulus cloud fraction observed for the strongest subsidence rates then indicates the dominance of LTS over subsidence as a predictor of cloudiness, similar to findings for stratocumulus cloud fields.

#### 4.2. SST and Moisture

SST is an important driver in the breakup of marine stratocumulus to shallow cumulus clouds in the tropics. Past studies agree on a decrease in cloud fraction with increasing SST (Klein & Hartmann, 1993; Qu et al., 2015; Stein et al., 2017), although they disagree on the underlying mechanism. A possible physical mechanism explaining the robust negative correlation is the increase in surface moisture fluxes with increasing SST and a deepening of the trade wind boundary layer. The deepening response may result in increased entrainment of warm and dry free tropospheric air into the cloud layer, which reduces cloudiness (Rieck et al., 2012). A second idea is that SST increase enhances the humidity contrast between the surface and the free troposphere, leading to increased mixing of drier free tropospheric air into the boundary layer and reduced cloud fraction (van der Dussen et al., 2015). A third proposed explanation is that a warmer SST increases the efficiency of entrainment (larger buoyancy flux per unit cloud depth), requiring thinner and smaller clouds to maintain a constant cloud top entrainment rate (Bretherton & Blossey, 2014). Finally, it has also been argued that the decrease of stratocumulus amount with SST may simply be due to a negative correlation between LTS and SST (Eitzen et al., 2011; Kubar et al., 2012).

All stated mechanisms are strongly coupled to the lower tropospheric moisture motivating its separate consideration in our study. We note that moisture influences shallow clouds in many different ways.



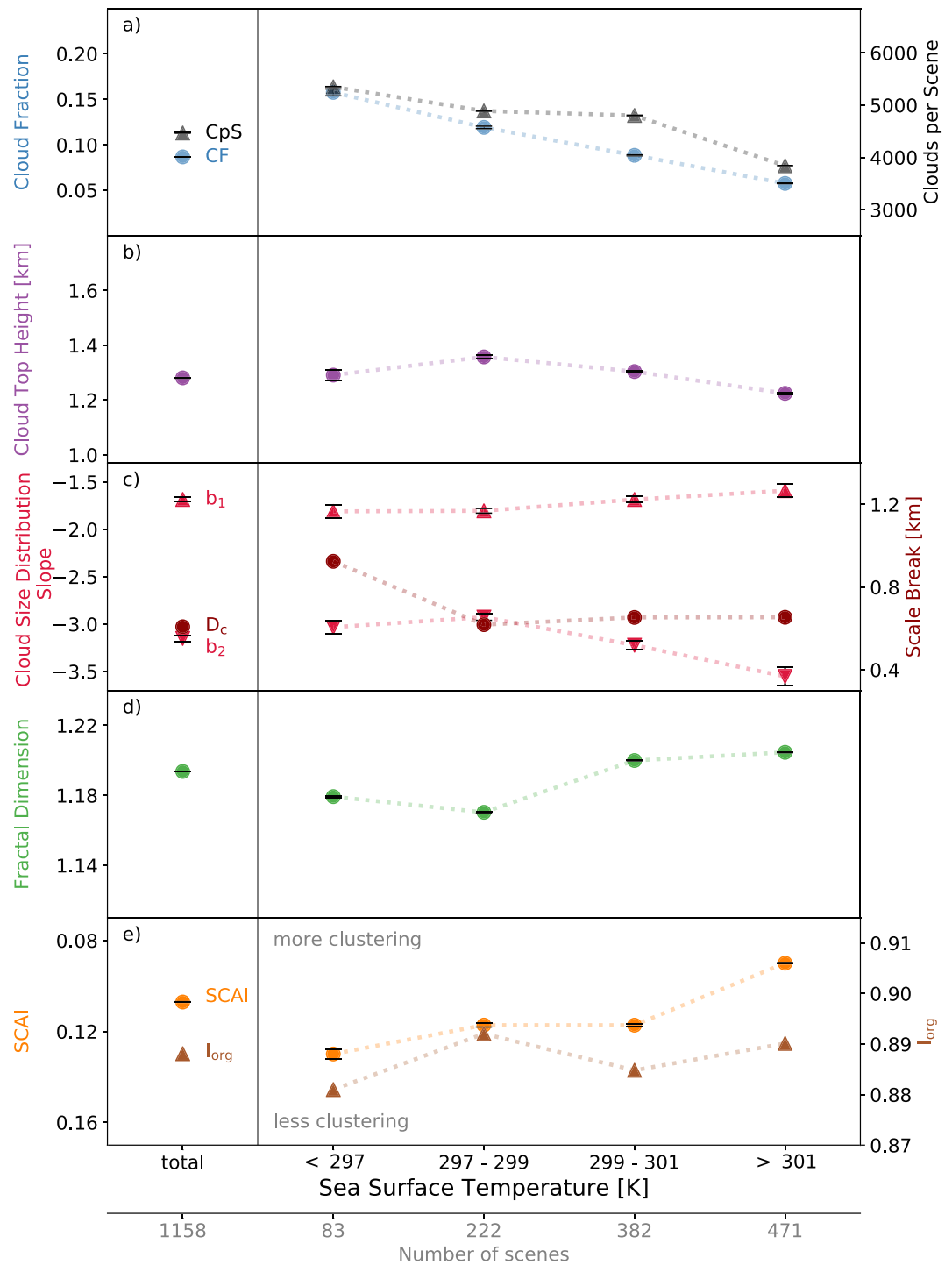


Figure 8. Same as Figure 6, but for sea surface temperature.

Surface moisture fluxes introduce moisture to the well-mixed subcloud layer, which builds a reservoir of moisture that potentially is transferred into the cloud layer and forms clouds. On the other hand, advected cold air can decrease the lower tropospheric moisture in the trade wind region. Similarly, entrainment of warm and dry free-tropospheric air at the top of the cloud layer can decrease the moisture content in the cloud layer. The relative importance of these mechanisms is the subject of ongoing research. MODIS-Terra provides estimates of the TCWV, which are concurrent with ASTER

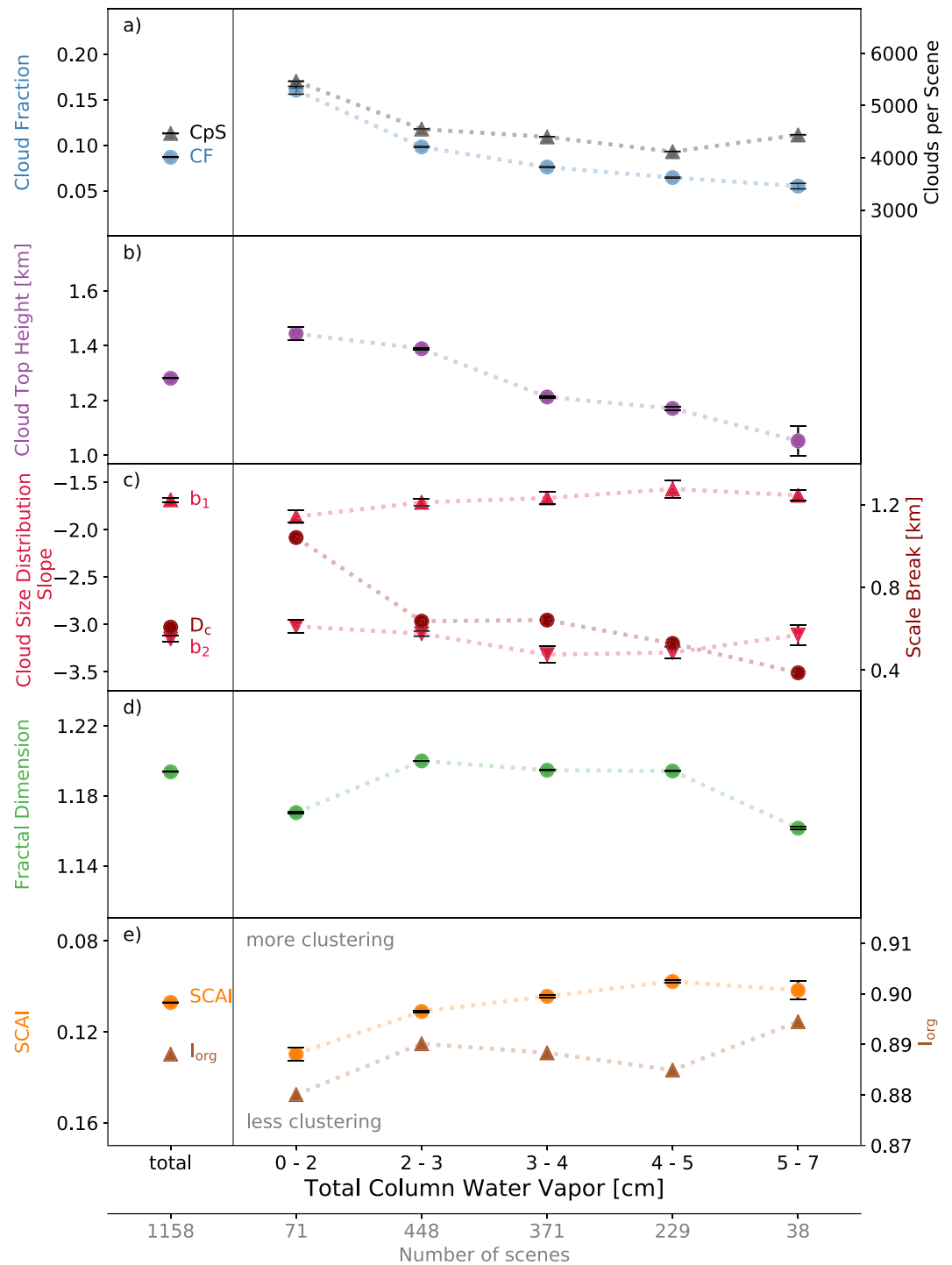


Figure 9. Same as Figure 6, but for total column water vapor.

observations and are therefore used in the present study. Changes in TCWV are largely determined by water vapor located between the top of the well-mixed subcloud layer and the height of the triple-point isotherm (Stevens et al., 2018). An increase especially in water vapor above cloud tops can increase the absorption of outgoing longwave radiation and thus change the temperature profile, cloud top subsidence, and cloud top entrainment rates, all leading to a change in cloud field properties (Myers & Norris, 2013).

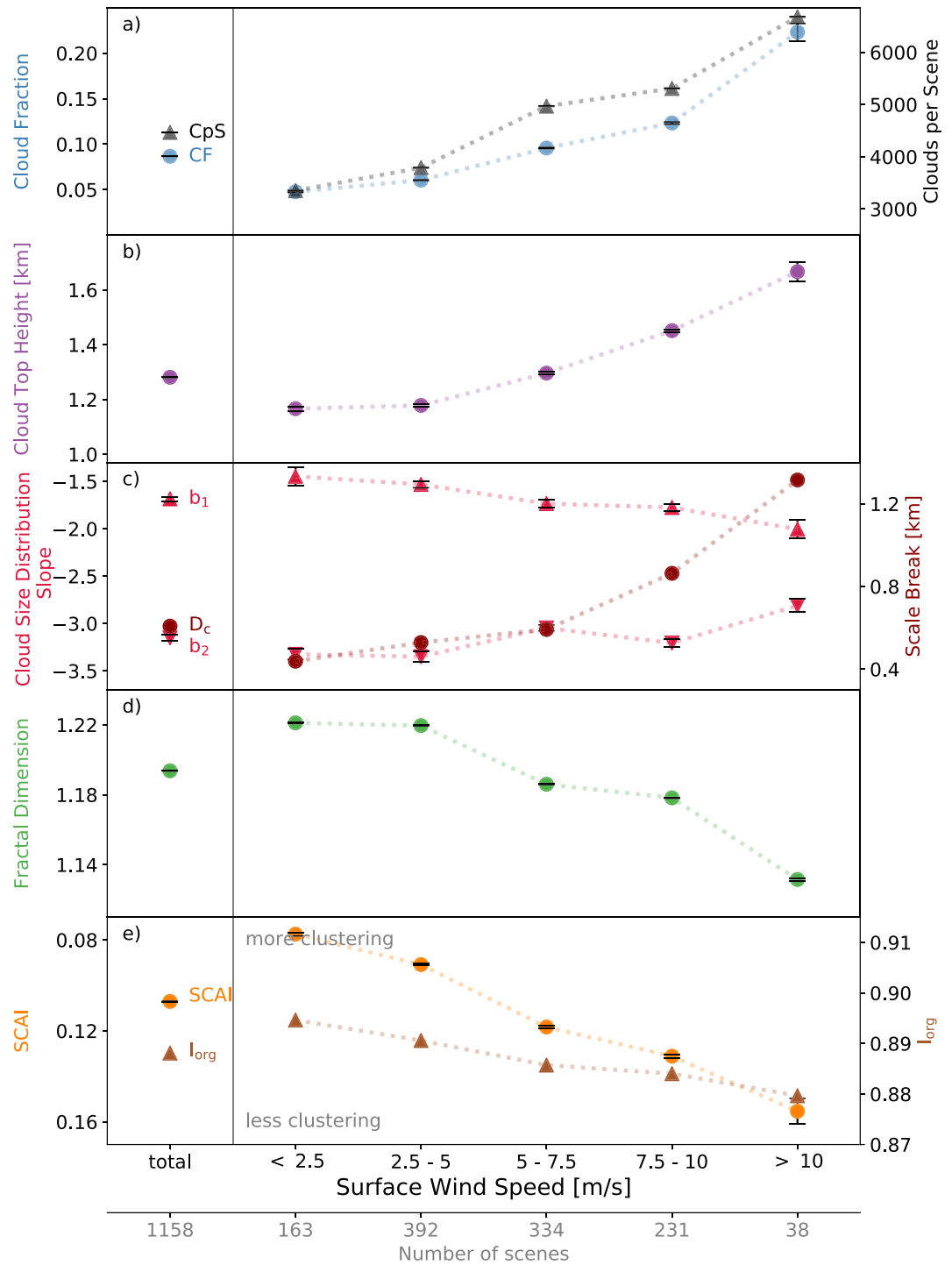
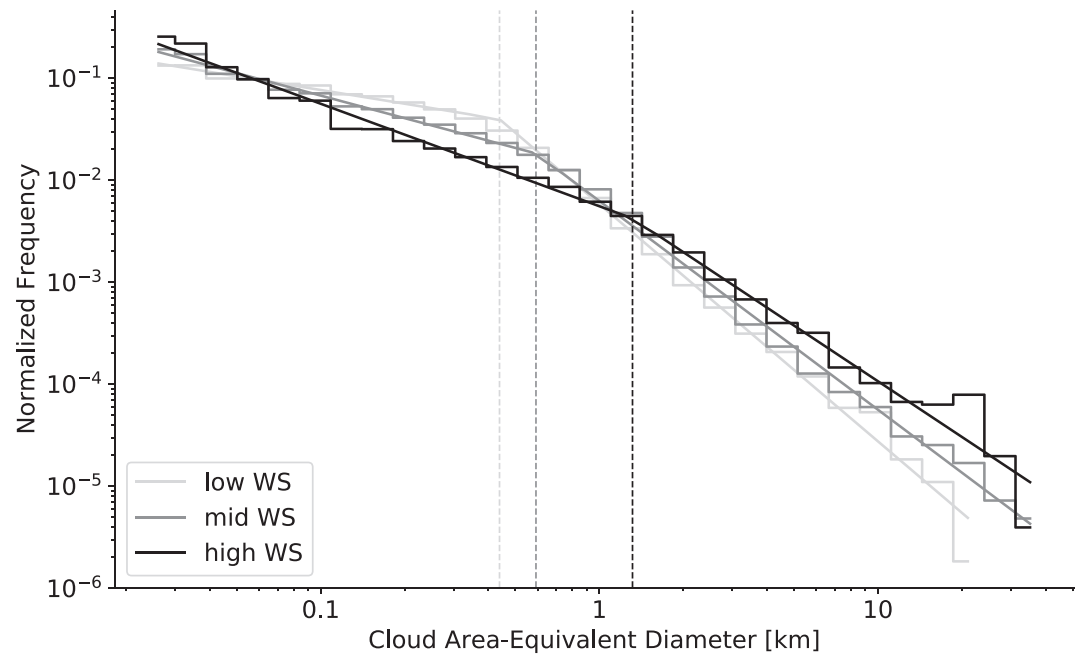


Figure 10. Same as Figure 6, but for surface wind speed.

Figures 8 and 9 show shallow cumulus cloud field properties as a function of SST and TCWV. From ASTER observations, we can confirm the decrease of cloud fraction with increasing SST as well as with increasing TCWV, a feature that all mentioned mechanisms have in common. The decrease between the coldest and warmest SST bin and the decrease from the driest to the moistest bin are both about 10%, which is approximately the same magnitude as the overall cloud fraction increase with LTS (see Figure 6). The rate of decrease in shallow cumulus fraction with SST is 1–2%/K, which is smaller than the SST sensitivities previously



**Figure 11.** Cloud size distributions under low (<2.5 m/s), middle (5–7.5 m/s), and high (>10 m/s) wind speed (WS) cases. Steps display the size distributions, solid lines the double power laws from linear regression, and the dashed lines depict the corresponding scale breaks.

observed in stratocumulus. The reported SST sensitivities are  $-5\%/K$  in Klein and Hartmann (1993),  $-3.4\%/K$  in Eitzen et al. (2011),  $-6.5\%/K$  in Kubar et al. (2012), and  $-1.3\%/K$  to  $-3.7\%/K$  in Qu et al. (2015). Similar to LTS relations, we attribute the cloud fraction changes with SST and TCWV to relative changes in the frequency of certain cloud sizes and to the overall decrease in the total number of clouds. With higher SST and TCWV the scaling parameters and the scale break size indicate a reduced amount of large clouds and only a slight increase in the amount of small clouds. The fractal dimension shows a small overall increase with SST, in line with the general finding that smaller clouds tend to be more irregular in our data set. In addition, the cluster indices show a change in the spatial distribution toward stronger clustering of clouds with increasing SST and TCWV. Reasons for and implications from this relation, however, are subjects of ongoing investigations.

Neglecting the coldest SST bin, CTHs decrease as SST and TCWV increase, showing especially a strong decrease of about 400 m from the driest to the moistest bin. A decrease in CTHs seems inconsistent with the surface-flux desiccation mechanism present in the simulations of Rieck et al. (2012), whereby increased moisture fluxes produce fewer but deeper cumulus clouds that carry more liquid water and have higher tops. The observed lowering of cumulus tops with SST, however, appears consistent with the entrainment liquid-flux adjustment feedback described in Bretherton and Blossey (2014). According to their model simulations, surface fluxes and turbulence intensify with increasing SST. However, stronger turbulence induces a stronger mixing of dry free tropospheric air into the cloud layer at the trade wind inversion layer. The dry and warm air leads to cloud thinning and lower cloud tops, which we can observe in the ASTER data set.

### 4.3. Surface Easterly Trade Winds

The tropical ocean in the trade wind region provides the moisture supply for the shallow cumulus cloud layer. The trade winds themselves regulate the moisture transport from the surface upwards by surface fluxes of heat, moisture, and momentum and thereby have a controlling role on the development and characteristics of shallow cumulus cloud fields. In an early observational study by Klein (1997), wind speed and surface wind stress were found to positively correlate with low-cloud amount in the tropical eastern Pacific. Similarly, Brueck et al. (2015) showed that wind speed has the best correlation with MODIS monthly mean low-cloud amount in the North Atlantic trades.

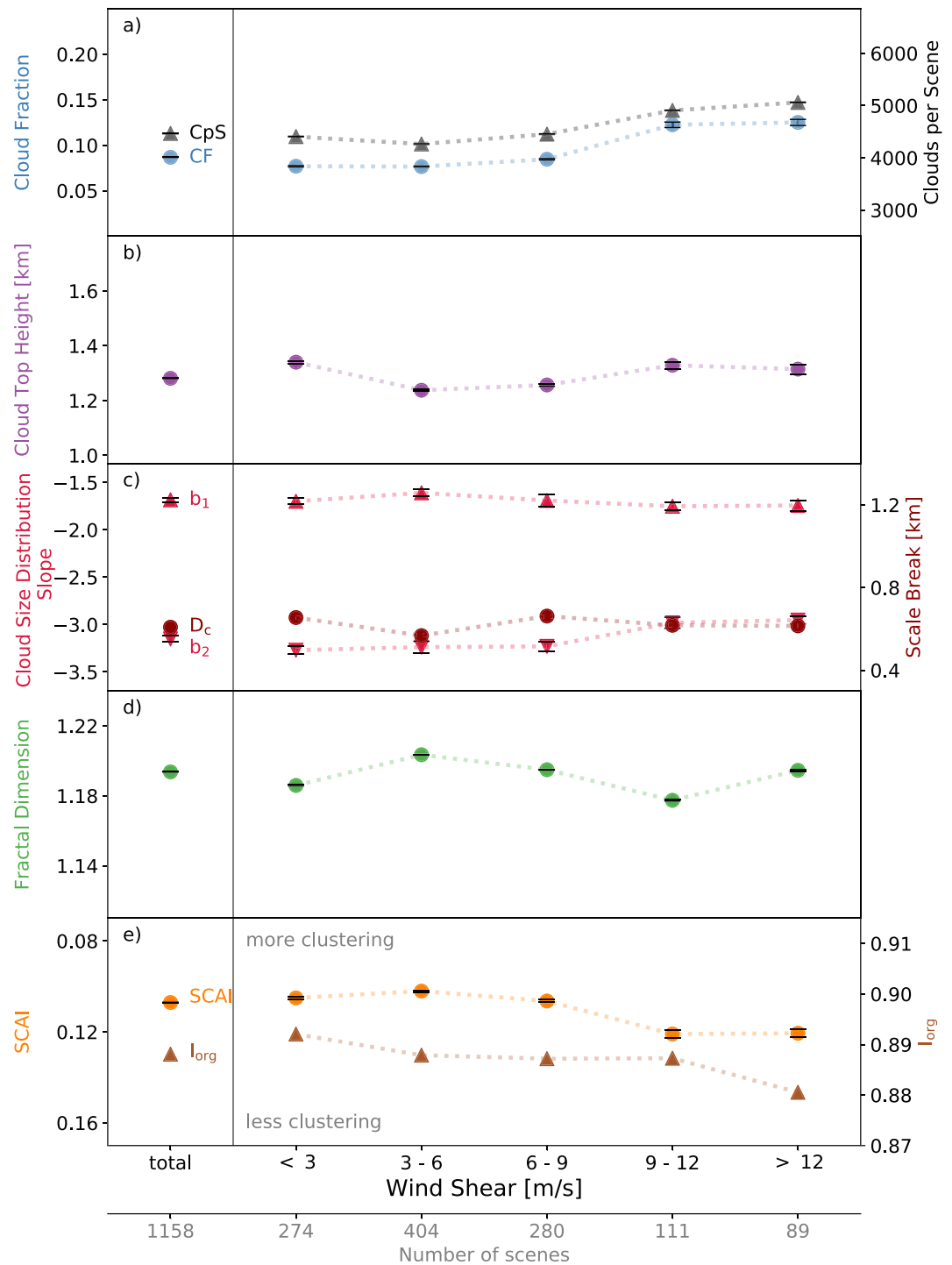


Figure 12. Same as Figure 6, but for wind shear.

The physical and dynamical mechanisms involved in the coupling between the trades typical surface easterly winds and the macrophysical properties of shallow cumulus cloud fields have been subject to several observational and modeling studies. Using ground-based radar data from the RICO field campaign, Nuijens et al. (2009) observed that periods of stronger shallow cumulus precipitation are characterized by deeper and moister layers and stronger easterlies, concluding that a more humid environment promotes deeper clouds and the humidity itself is regulated by wind speed. In addition, stronger surface winds frequently

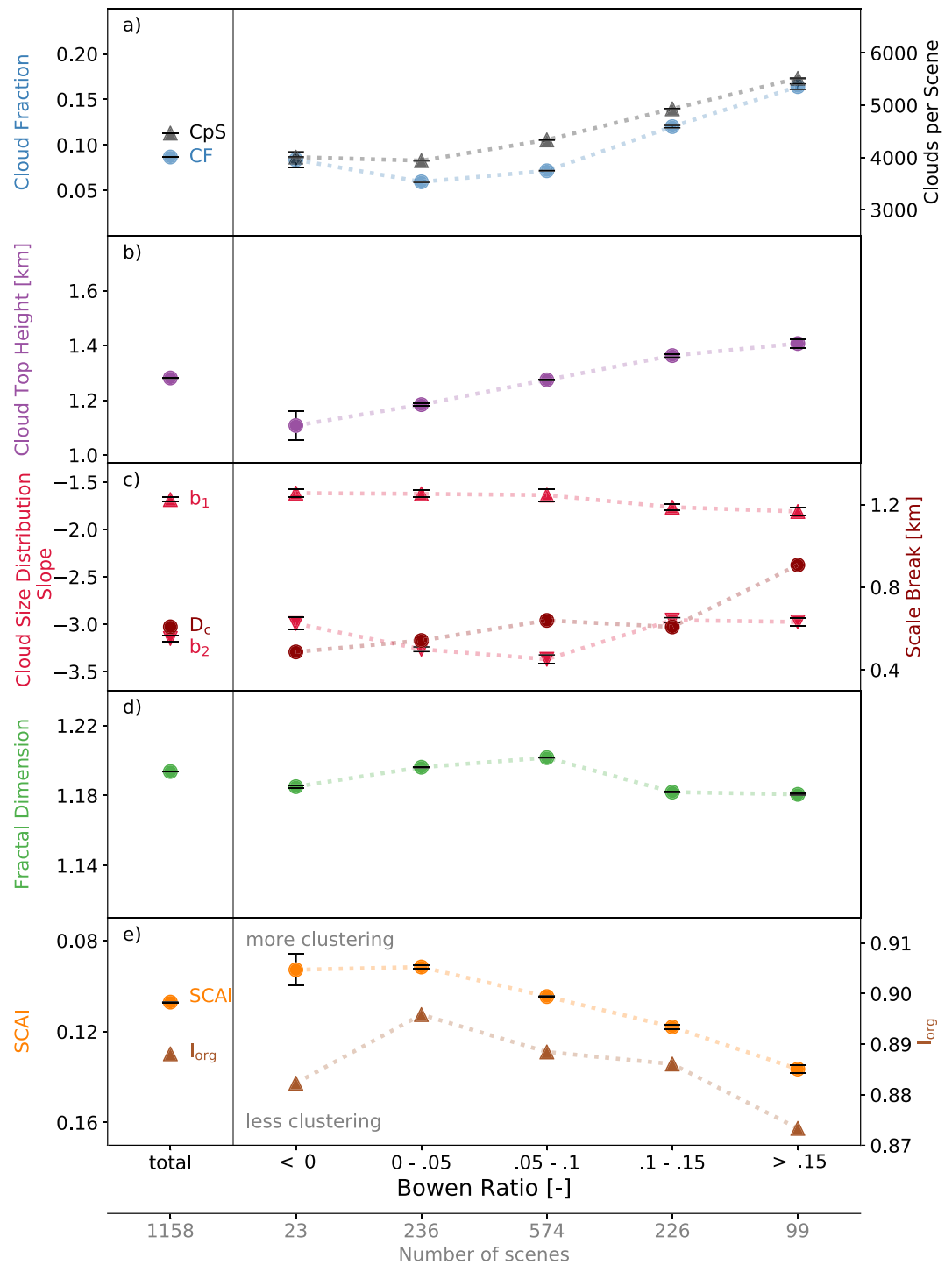



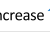
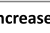
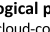
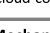

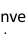
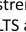
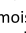
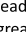
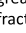

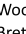


Figure 13. Same as Figure 6, but for Bowen ratio.

occur in combination with horizontal cold air advection, which increases the upward buoyancy flux and promotes more clouds by destabilizing the surface-atmosphere interface (Klein, 1997; Norris & Iacobellis, 2005). Simulations of an idealized nonprecipitating shallow cumulus case by Nuijens and Stevens (2012) showed considerable deepening of the cloud layer at higher wind speeds. Applying concepts from bulk theory, the deepening is a necessary response to allow the surface buoyancy flux to remain constant without further moistening the subcloud layer in its adjustment to a new equilibrium. In the simulation,

ASTER Observations	Cloud Size and Top Height								
	Cloud Fraction	Increase ↑ Decrease ↓							
Increased meteorological parameter (cloud-controlling factor)	Lower Tropospheric Stability (LTS)	Subsidence Rate	Sea Surface Temperature (SST)	Total Column Water Vapor (TCWV)	Surface Wind Speed	Wind Shear	Bowen Ratio		
Mechanism	Boundary layer inversion strengthens with LTS and traps moisture, leading to greater cloud fraction.	Subsidence limits cloud growth, but opposing LTS signal (increasing cloud fraction) overcompensates for the reduction in cloud fraction.	Higher SST increases surface moisture fluxes. A strong moisture gradient leads to an increased entrainment efficiency at the boundary layer inversion and to cloud thinning and lower cloud tops (entrainment liquid-flux adjustment feedback).		Increase in surface fluxes of heat, moisture, and momentum with wind speed deepens the boundary layer, enabling larger and deeper clouds.	Wind shear tilts especially the deeper clouds and increases projected cloud fraction.	The Bowen ratio controls cloud base mass flux by setting the thermodynamic efficiency of the moist convective heat cycle.		
References (only the most relevant one)	Wood and Bretherton (2006)	Myers and Norris (2013)	Bretherton and Blossey (2014), Rieck et al. (2012)		Nuijens and Stevens (2012)	Neggert et al. (2003)	Sakradzija and Hohenegger (2017)		

**Figure 14.** Schematic summary of correlations between cloud field properties—cloud size, cloud top height, and cloud fraction—and large-scale meteorological parameters as observed in ASTER images. The arrows indicate the change in cloud properties with a change in the meteorological parameter from an initial (light blue) to an increased value (dark blue). Possible mechanisms are introduced in the corresponding references.

the cloud layer deepens, enabling deeper and larger clouds to form. Wind speed is positively correlated with wind shear, and enhanced wind shear might further enhance the projected cloud cover as deeper and larger clouds get tilted with height (Brueck et al., 2015; Neggers et al., 2003).

While Nuijens and Stevens (2012) promote a wind speed-regulated and deepening trade wind boundary layer, the LES study by Bretherton et al. (2013) similarly finds larger clouds with increasing wind speed, but a limited variation of boundary layer depth. In the precipitation-permitting study of Bretherton et al. (2013), higher wind speed leads to increased surface-driven turbulence, increased latent heat flux, and thus more cloud. This study illustrates the so-called-precipitation governor mechanism, which limits inversion height changes. As cumulus clouds become deep enough, they precipitate more efficiently, which reduces the supply of liquid water to the inversion layer and prevents a significant deepening of the cloud layer.

From analyzing ASTER images we do find the strongest and most systematic variation in cloud field properties with wind speed. Figure 10 shows a strong increase in cloud fraction by about 15% from low to high wind speed situations. Similarly, the CTHs increase on average by 400 m, indicating deeper clouds, as the cloud base height over the ocean is fairly constant. Deeper clouds coincide with a higher frequency of large clouds, which is obvious from the opposing changes of the double power law scaling parameters  $b_1$  and  $b_2$ . The scale break size  $D_c$  increases with increasing wind speed from 440 m to about 1,300 m, similarly implying a shift in the size distribution toward larger clouds. Visually, the change in the shape of the distribution becomes even clearer in Figure 11 where the distribution is shown for the lowest, middle, and highest wind speed bin. Taking the actual cloud area instead of the commonly used cloud area-equivalent diameter results in the same qualitative change in the cloud size distribution (not shown here) confirming the robustness of our findings to the different definitions for cloud size.

Increasing cloud sizes and the deepening of the cloud layer is consistent with the nonprecipitating shallow cumulus simulations of Nuijens and Stevens (2012) and thus confirms a primarily wind speed-regulated boundary layer. Shallow cumulus precipitation unfortunately cannot be diagnosed from passive satellite measurements, and even current space-borne radars would miss a large portion of the light rains encountered in these clouds, but ground-based radar data show that shallow precipitation is indeed ubiquitous (Nuijens et al., 2009). Nevertheless, the observed CTH increase implies that the precipitation governor mechanism of Bretherton et al. (2013) seems too weak to prevent the cloud layer deepening response in our data set.

The fractal dimension  $d$  in Figure 10c decreases with wind speed, indicating a transition from ragged shapes to more compact and smooth cloud shapes ( $d$  close to 1). In a calm environment, enhanced entrainment of dry air at cloud edges might lead to ragged cloud edges. This idea is supported by a parameterization of moist convection in a rising plume model by Neggers (2015), where the entrainment is assumed to decrease with increasing plume size. We hypothesize that stronger winds introduce an anisotropy in cloud growth, inhibiting it upwind and promoting it downwind. As a result, individual clouds may be elongated in the wind direction or tilted out of the vertical, as wind shear also tends to increase with wind speed. It is therefore not difficult to imagine how the structure imposed on the flow by stronger winds could result in smoother cloud shapes with smaller fractal dimensions.

According to the last panel in Figure 10, wind speed influences not only cloud shapes but also the spatial distribution of clouds. The increase in SCAI as well as the decrease in  $I_{\text{org}}$  with increasing wind speed means that cloud fields are less aggregated in high wind speed cases. One can easily imagine that strong winds inhibit organized convection, although the exact mechanisms are unclear at this stage. We studied the change in SCAI in more detail as it is governed by two variables, the total number of clouds in an image and the average distance between all clouds (see equation (7)). We found that the increase in SCAI with increasing wind speed in low-wind speed situations is due to an increase in the total number of clouds. We hypothesize that the increase in wind speed goes along with an increase in moisture being mixed upward, which provides the basis for new cumulus clouds to develop. On the other hand, the increase in SCAI in high-wind speed situations results from a strong increase in the average distance between the clouds, which clearly dominates the calculated SCAI values as the number of clouds decreases simultaneously. Taking into account that clouds also tend to be larger in the case of high surface winds, we propose that larger clouds suppress convection in close proximity, leading to higher average distances between clouds in a fixed domain.

The variation of cloud field properties with wind speed might include wind shear effects too, as wind speed and wind shear are positively correlated (Brueck et al., 2015). We define a scene-average wind shear as the absolute value of the wind vector difference between 700 and 1,000 hPa. Although it covaries with wind speed, shear itself induces little systematic variation in cloud properties, as most cloud field properties simply fluctuate around their mean values (see Figure 12). Only cloud fraction exhibits a 4% increase at the highest wind shear values above 9 m/s, most likely due to the tilting of cumulus towers (Neggers et al., 2003). The observed minor changes are consistent with the observational study by Brueck et al. (2015) and the modeling study by Nuijens et al. (2015), both claiming that wind shear plays a minor role in regulating cloud fields in the trade wind region.

In conclusion, our results support the hypothesis of a deepening response of the trade wind boundary layer to increasing surface wind speed. Clouds are found to be deeper and horizontally larger leading to an increase in cloud fraction. This result is in agreement with studies by Nuijens and Stevens (2012) and Brueck et al. (2015) where wind speed is found to be the major control factor on low-level cloudiness in observational data at the BCO. Both studies provide a physical explanation for the observed changes by linking higher wind speeds to enhanced evaporation over the ocean that alters the surface fluxes. Surface sensible and latent fluxes are governed by wind speed and the difference in temperature and moisture between the surface and cloud base. An increase in wind speed therefore results in an enhanced moisture and mass flux into the cloud layer, jointly leading to a change in cloud field properties.

#### 4.4. Bowen Ratio

The influence of wind speed-driven surface fluxes on shallow convection is subject to a recent LES study from Sakradzija and Hohenegger (2017), which investigates parameters that influence the distribution of cloud-base mass flux under time-invariant profiles of subsidence, horizontal advection, background wind, and a fixed SST. They concluded that the Bowen ratio ( $B$ ), the ratio of the surface sensible heat flux to the latent heat flux, controls the shape of the cloud-base mass flux distribution by setting the thermodynamic efficiency of the moist convective heat cycle. While the surface wind speed is correlated with both of the surface fluxes, with a Pearson correlation coefficient for latent heat flux  $r_l=0.7$  and for sensible heat flux  $r_s=0.4$ , it is uncorrelated with the corresponding Bowen ratio,  $r_B=0.1$ , which thus can be viewed independently. Sakradzija and Hohenegger (2017) found that cloud area is distributed similarly to cloud-base mass flux with the distribution slopes systematically changing as  $B$  increased from a baseline value of 0.03 to 0.24 and to 0.33.



Motivated by this study, we show variations in ASTER cloud field properties, in particular the cloud size distribution, with Bowen ratio in Figure 13. We derive  $B$  from ERA-Interim surface fluxes and find a narrow distribution of  $B$  around the average value of 0.08. Furthermore, about 2% of the values are negative, which, however, are of minor importance as they are not covered by the LES runs. According to Sakradzija and Hohenegger (2017), typical values for  $B$  over the Atlantic ocean during the RICO campaign were about 0.05. In Figure 13, such a low value for  $B$  corresponds to low cloud fractions around 7%, CTHs of about 1.2 km, and rather aggregated cloud fields. With increasing  $B$  the cloud fraction and CTH increase, and the scaling parameters and scale break size indicate a higher frequency of large clouds. Higher cloud tops and the changes in the cloud size distribution are in qualitative agreement with the LES results, where cloud-base mass flux distribution shifts toward higher values with  $B$ . The distribution of cloud-base areas simulated by Sakradzija and Hohenegger (2017) had a scale break around  $10^5 \text{ m}^2$ , which compares reasonably well with the scale break size of  $2.7 \cdot 10^5 \text{ m}^2$  observed in our data set (see Figure 5b). The fractal dimension on the other hand does not show any systematic behavior.

In LES, ocean surface winds set the rate of heat and moisture that is transported upward into the cloud layer potentially forming clouds. Based on the preceding analysis of wind speed influence on ASTER cloud field properties and the theoretical concept of shallow moist convection by Sakradzija and Hohenegger (2017), we conclude that wind speed indeed has a major control, possibly through altering the ratio of the surface fluxes. The fact that the influence of surface wind speed and not that of  $B$  shows the strongest changes in cloud field properties might be the result of the insufficient accuracy of ERA-Interim reanalysis data for this study. The small range of  $B$  values might be a further limiting factor.

#### 4.5. Schematic Summary of Observed Correlations

In Figure 14 we summarize the observed effects of cloud-controlling factors on shallow cumulus clouds. In particular, we illustrate how shallow cumuli change in size, CTH, and how the cloud fraction evolves. The sketched change of a cloud corresponds to the average change with increasing value of a given large-scale meteorological parameter. For every parameter we hypothesize the dominant mechanism and provide the most relevant literature. We emphasize again that surface wind speed shows the strongest signal of all cloud-controlling factors in our study, followed by LTS, Bowen ratio, SST, and TCWV. The subsidence rate and wind shear, in contrast, do not show significant influences on cloud field properties.

### 5. Summary and Conclusions

We investigated the influence of large-scale meteorological fields on shallow cumulus cloud fields as observed in 1,158 high-resolution satellite images from ASTER, which were collected over the tropical Atlantic and Pacific oceans between 2000 and 2007. The high spatial resolution of the ASTER sensors facilitates the investigation of clouds on scales smaller than 1 km. We characterize cloud fields observed in ASTER imagery by their macrophysical properties and go beyond most prior studies in covering not only cloud fraction but also CTH, cloud size distribution, fractal dimension, and horizontal cloud distribution or spatial clustering. We investigate the variation of these cloud properties with meteorological parameters from ERA-Interim, specifically subsidence rate, LTS, SST, TCWV, surface wind speed, wind shear, and the Bowen ratio.

From 1,158 cloud images an average cloud fraction of 8.7% is calculated, with 90% of the individual scenes having a cloud fraction below 20%. The distribution of scene-average CTHs exhibits a single peak just below the average CTH of 1.3 km. The ensemble of clouds is characterized by the cloud size distribution and the fractal dimension. Estimating the power law scaling parameter of cloud size distributions from linear fits to histograms in a log-log plot gives predictably different results, depending on the cloud size measure (equivalent diameter or area) and binning scheme (linear or logarithmic) used. We show that the distribution of shallow cumulus clouds can be well described by a double power law with the scaling parameters of  $b_1 = -1.68$  for small cloud sizes and  $b_2 = -3.12$  representing the large cloud sizes. A characteristic scale break at about 0.6 km is found in agreement with previous studies reporting values ranging from 0.5 km to about 1 km. We argue that the large range of scaling parameters stated in the literature is partly due to different fitting strategies and in some cases due to insufficiently small data samples. The derived fractal dimension of  $d = 1.19$  means that the sampled clouds are rather compact and exhibit smoother shapes compared to previous studies. The analysis of the cloud spatial distribution reveals that shallow cumulus clouds appear almost exclusively in the form of clustered

cloud fields. The aggregation index SCAI exhibits a skewed distribution indicating a higher occurrence of clustered cloud fields and the organization index  $I_{\text{org}}$  strongly confirms the overall tendency toward clustered cloud fields with a narrow distribution around the average value of  $I_{\text{org}} = 0.89$ .

Based on the variation of cloud field properties, we evaluated the role of large-scale meteorological parameters in controlling shallow clouds. Large-scale subsidence is one of the key features in the trade wind region, which provides the general conditions for the development of shallow cumulus cloud fields. Nevertheless, we find only weak relationships between cloud field properties and the subsidence rate. It is found that shallow cumulus amount shows the same overall dependencies on control factors as the more often studied marine stratocumulus amount. Specifically, shallow cumulus fraction steadily increases with increasing LTS, increasing surface wind speed, decreasing SST, decreasing TCWV, and increasing Bowen ratio. Clouds tend to be slightly larger in very stable situations and under moderate subsiding motion, leading to an increase in cloud fraction. Analyzing variations in shallow cumulus cloud field properties with SST and TCWV proved known behavior from LES studies, such as reduced cloud cover, a higher frequency of small clouds, and a higher cluster tendency with increasing SST and TCWV. Shallow cumulus cloud fields seem to respond to meteorology in a similar way as stratocumulus, although the absolute sensitivities to control factors are smaller.

Prominent trade winds, however, emerge as the most powerful control factor, as all cloud macrophysical properties show the strongest and most systematic variation with change in the strength of surface wind speed. Our observations are consistent with the hypothesis from modeling studies that surface wind speed drives the surface fluxes and therefore the moisture and momentum transport into the cloud layer, leading to a deepening of the trade wind boundary layer. Strong winds produce large clouds with smooth and compact cloud shapes and also higher cloud cover. We hypothesize that smoother cloud shapes might arise from strong winds coupled with increased shear imposing an anisotropy on cloud growth, inhibiting it upwind and promoting it downwind, resulting in more regular elongated shapes and thereby explaining the observed decrease in fractal dimension. CTH also increases with wind speed by a significant amount, lending observational support to the deepening response present in an LES study of a nonprecipitating trade cumulus case by Nuijens and Stevens (2012). In situations of low surface wind speed we observe a tendency toward clustered cloud fields, while strong winds seem to inhibit cloud fields from organizing into clusters or arcs. Although wind speed and wind shear are correlated, we cannot find any significant variation in cloud field properties with the bulk wind shear and conclude that wind shear is of minor importance in regulating shallow cumulus clouds in the trade wind boundary layer.

In addition, we investigated the relationships between cloud field properties and the Bowen ratio, which is related to wind speed through the surface fluxes. The Bowen ratio is a potential new control factor proposed by a recent LES study of Sakradzija and Hohenegger (2017) to control the shape of the cloud area distribution by setting the thermodynamic efficiency of the moist convective heat cycle. The change in the cloud size distribution slopes, the shift toward larger clouds and larger cloud fractions, and the increase in CTH observed in our data set with increasing Bowen ratio all qualitatively agree with the LES simulations, suggesting that the effect of this parameter on trade-wind cloudiness merits further investigation.

This study lends observational support to some of the proposed control mechanisms of shallow cumulus clouds. However, we explicitly note that relationships do not imply any physical or dynamical causality but merely support ideas on possible mechanisms and give room for new hypothesis. Neither surface wind speed, nor the subsidence of air masses or further large-scale meteorological variables stand out alone as the main driver of the observed cloud fields. The covariance of these parameters is a further complicating factor and needs to be studied in more detail. Understanding control parameters more accurately can improve convective parametrization schemes in general circulation and large-eddy models and eventually reduce some uncertainty in climate projections.

## Appendix A: Dependence of Scaling Parameters on Cloud Size Measure and Binning Method

Cloud size distributions are often assumed to follow a power law, but past studies estimated scaling parameters in different ways, which can lead to confusion. In the following, we explicitly derive the mathematical relations between the scaling parameters resulting from different binning methods and different cloud size measures.

We assume that the cloud size density  $n(D)$  of the cloud area-equivalent diameter  $D$  follows a power law:

$$n(D) = c \cdot D^b. \quad (\text{A1})$$

The total number of clouds  $N$  is the integral over the cloud size density  $N = \int_0^\infty n(D) dD$  and accordingly  $n(D) = dN/dD$  and  $n(\log(D)) = dN/d\log(D)$ .

Independent of the exact definition of the cloud size measure, the integral  $\int_0^\infty n(D) dD$  is a conserved quantity. Therefore, we can relate  $n(\log(D))$ ,  $n(A)$  and  $n(\log(A))$  to  $n(D)$ :

$$\int_0^\infty n(D) dD = \int_0^\infty n(x) dx. \quad (\text{A2})$$

For  $x = \log(D)$  and  $\frac{dx}{dD} = \frac{1}{D \cdot \ln(10)}$ ,

$$\begin{aligned} n(\log(D)) &= n(D) \cdot D \cdot \ln(10) \\ &= c \cdot \ln(10) \cdot D \cdot D^b \\ &= c' \cdot D^{b+1}. \end{aligned} \quad (\text{A3})$$

For  $x = A = \frac{\pi}{4} \cdot D^2$  and  $\frac{dx}{dD} = \frac{\pi}{2} \cdot D$ ,

$$\begin{aligned} n(D) &= n(A) \cdot \frac{dA}{dD} \\ &= n(A) \cdot \frac{\pi}{2} \cdot D, \\ n(A) &= n(D) \cdot \frac{2}{\pi} \cdot D^{-1} \\ &= c \cdot \frac{2}{\pi} \cdot D^{b-1} \\ &= c'' \cdot A^{\frac{b-1}{2}}, \end{aligned} \quad (\text{A4})$$

for  $x = \log(A) = \log(\frac{\pi}{4} D^2)$  and

$$\begin{aligned} \frac{dx}{dD} &= \frac{1}{\frac{\pi}{4} D^2 \cdot \ln(10)} \cdot \frac{\pi}{2} D \\ &= \frac{2}{\ln(10)} D^{-1}, \end{aligned} \quad (\text{A5})$$

$$\begin{aligned} n(\log(A)) &= n(D) \cdot \frac{\ln(10)}{2} D \\ &= c \cdot \frac{\ln(10)}{2} \cdot D^{b+1} \\ &= c''' \cdot A^{\frac{b+1}{2}}. \end{aligned} \quad (\text{A6})$$

#### Acknowledgments

The study was supported by the International Max Planck Research School on Earth System Modelling (IMPRS-ESM), Hamburg, and the Universität Hamburg. The contribution of Stefan A. Buehler was supported by the Deutsche Forschungsgemeinschaft (DFG, German Research Foundation) under Germany's Excellence Strategy — EXC 2037 'Climate, Climatic Change, and Society' — Project Number: 390683824, contributing to the Center for Earth System Research and Sustainability (CEN) of Universität Hamburg. The work of Ákos Horváth was supported by the BMBF project HD (CP)<sup>2</sup> (Contract O1LK1505D). We would like to thank Chris Bretherton, Matthias Brueck, and Cathy Hohenegger for useful discussions on the structure and prevailing dynamical processes in the trade wind boundary layer. Theresa Mieslinger would like to thank Lukas Kluff and Oliver Lemke for their IT support. The authors declare no financial conflicts of interests. The ASTER LIB and the MODIS data products were retrieved from the online Data Pool, courtesy of the NASA Land Processes Distributed Active Archive Center (LP DAAC), USGS/Earth Resources Observation and Science (EROS) Center, Sioux Falls, South Dakota ([https://lpdaac.usgs.gov/data\\_access/data\\_pool](https://lpdaac.usgs.gov/data_access/data_pool)). We acknowledge ECMWF and the Copernicus Climate Change Service for providing access to the ERA-Interim data set through their public data portal. The Python functions implemented for calculating cloud field statistics are freely available within the python package *typhon*, subpackage *cloudmask* (<http://doi.org/10.5281/zenodo.1300319>).

#### References

- Abrams, M., Hook, S., & Ramachandran, B. (2000). ASTER user handbook. Advanced Thermal Emission and Reflection Radiometer, NASA JPL. [https://asterweb.jpl.nasa.gov/content/03\\_data/04\\_Documents/aster\\_user\\_guide\\_v2.pdf](https://asterweb.jpl.nasa.gov/content/03_data/04_Documents/aster_user_guide_v2.pdf)
- Baum, B. A., Menzel, W. P., Frey, R. A., Tobin, D. C., Holz, R. E., Ackerman, S. A., & Yang, P. (2012). MODIS cloud-top property refinements for Collection 6. *Journal of Applied Meteorology and Climatology*, 51(6), 1145–1163. <https://doi.org/10.1175/JAMC-D-11-0203.1>
- Benner, T. C., Curry, J. A., & Webster, P. J. (1998). Characteristics of small tropical cumulus clouds and their impact on the environment. *Journal of Geophysical Research*, 103, 28,753–28,767.
- Berrisford, P., Dee, D., Poli, P., Brugge, R., Fielding, K., Fuentes, M., & Simmons, A. (2011). *The ERA-Interim archive Version 2.0*. (No. 1), UK: ECMWF.

- Bony, S., & Dufresne, J. L. (2005). Marine boundary layer clouds at the heart of tropical cloud feedback uncertainties in climate models. *Geophysical Research Letters*, *32*, L20806. <https://doi.org/10.1029/2005GL023851>
- Bretherton, C. S., & Blossey, P. N. (2014). Low cloud reduction in a greenhouse-warmed climate: Results from Lagrangian LES of a subtropical marine cloudiness transition. *Journal of Advances in Modeling Earth Systems*, *6*, 91–114. <https://doi.org/10.1002/2013MS000250>
- Bretherton, C. S., Blossey, P. N., & Jones, C. R. (2013). Mechanisms of marine low cloud sensitivity to idealized climate perturbations: A single-LES exploration extending the CGILS cases. *Journal of Advances in Modeling Earth Systems*, *5*, 316–337. <https://doi.org/10.1002/jame.20019>
- Brucek, M., Nuijens, L., & Stevens, B. (2015). On the seasonal and synoptic time-scale variability of the North Atlantic Trade Wind Region and its low-level clouds. *Journal of the Atmospheric Sciences*, *72*, 1428–1446. <https://doi.org/10.1175/JAS-D-14-0054.1>
- Cahalan, R. F., & Joseph, J. H. (1989). Fractal statistics of cloud fields. *Monthly Weather Review*, *117*(2), 261–272. [https://doi.org/10.1175/1520-0493\(1989\)117<0261:FSSOCF>2.0.CO;2](https://doi.org/10.1175/1520-0493(1989)117<0261:FSSOCF>2.0.CO;2)
- Clauset, A., Shalizi, C., & Newman, M. (2009). Power-law distributions in empirical data. *SIAM Review*, *51*(4), 661–703. <https://doi.org/10.1137/070710111>
- Dawe, J. T., & Austin, P. H. (2012). Statistical analysis of an LES shallow cumulus cloud ensemble using a cloud tracking algorithm. *Atmospheric Chemistry and Physics*, *12*(2), 1101–1119. <https://doi.org/10.5194/acp-12-1101-2012>
- Dee, D. P., Uppala, S. M., Simmons, A. J., Berrisford, P., Poli, P., Kobayashi, S., & Vitart, F. (2011). The ERA-Interim reanalysis: Configuration and performance of the data assimilation system. *Quarterly Journal of the Royal Meteorological Society*, *137*(656), 553–597. <https://doi.org/10.1002/qj.828>
- Eitzen, Z. A., Xu, K. M., & Wong, T. (2011). An estimate of low-cloud feedbacks from variations of cloud radiative and physical properties with sea surface temperature on interannual time scales. *Journal of Climate*, *24*(4), 1106–1121. <https://doi.org/10.1175/2010JCLI3670.1>
- Genkova, I., Seiz, G., Zuidema, P., Zhao, G., & Girolamo, L. D. (2007). Cloud top height comparisons from ASTER, MISR, and MODIS for trade wind cumuli. *Remote Sensing of Environment*, *107*(1–2), 211–222. (Multi-angle Imaging SpectroRadiometer (MISR) Special Issue/MISR Special Issue) <https://doi.org/10.1016/j.rse.2006.07.021>
- Gotoh, K., & Fujii, Y. (1998). A fractal dimensional analysis on the cloud shape parameters of cumulus over land. *Journal of Applied Meteorology*, *37*(10), 1283–1292. [https://doi.org/10.1175/1520-0450\(1998\)037<1283:AFDAOT>2.0.CO;2](https://doi.org/10.1175/1520-0450(1998)037<1283:AFDAOT>2.0.CO;2)
- Greenwald, T. J., Bennartz, R., Lebsock, M., & Teixeira, J. (2018). An uncertainty data set for passive microwave satellite observations of warm cloud liquid water path. *Journal of Geophysical Research: Atmospheres*, *123*, 3668–3687. <https://doi.org/10.1002/2017JD026738>
- Heus, T., & Seifert, A. (2013). Automated tracking of shallow cumulus clouds in large domain, long duration large eddy simulations. *Geoscientific Model Development*, *6*(4), 1261–1273. <https://doi.org/10.5194/gmd-6-1261-2013>
- Hinkelmann, L. M., Evans, K. F., Clothiaux, E. E., Ackerman, T. P., & Stackhouse, P. W. (2007). The effect of cumulus cloud field anisotropy on domain-averaged solar fluxes and atmospheric heating rates. *Journal of the Atmospheric Sciences*, *64*(10), 3499–3520. <https://doi.org/10.1175/JAS4032.1>
- Jiang, H., Feingold, G., Jonsson, H. H., Lu, M. L., Chuang, P. Y., Flagan, R. C., & Seinfeld, J. H. (2008). Statistical comparison of properties of simulated and observed cumulus clouds in the vicinity of Houston during the Gulf of Mexico Atmospheric Composition and Climate Study (GoMACCS). *Journal of Geophysical Research*, *113*, D13205. <https://doi.org/10.1029/2007JD009304>
- King, M. D., Menzel, W. P., Kaufman, Y. J., Tanre, D., Gao, B. C., Platnick, S., & Hubanks, P. A. (2003). Cloud and aerosol properties, precipitable water, and profiles of temperature and water vapor from MODIS. *IEEE Transactions on Geoscience and Remote Sensing*, *41*(2), 442–458. <https://doi.org/10.1109/TGRS.2002.808226>
- Klein, S. A. (1997). Synoptic variability of low-cloud properties and meteorological parameters in the subtropical trade wind boundary layer. *Journal of Climate*, *10*(8), 2018–2039. [https://doi.org/10.1175/1520-0442\(1997\)010<2018:SVOLCP>2.0.CO;2](https://doi.org/10.1175/1520-0442(1997)010<2018:SVOLCP>2.0.CO;2)
- Klein, S. A., Hall, A., Norris, J. R., & Pincus, R. (2018). Low-cloud feedbacks from cloud-controlling factors: A review. *Shallow clouds, water vapor, circulation, and climate sensitivity* (pp. 135–157), Space Sciences Series of ISSI, vol 65. Springer, Cham. [https://doi.org/10.1007/978-3-319-77273-8\\_7](https://doi.org/10.1007/978-3-319-77273-8_7)
- Klein, S. A., & Hartmann, D. L. (1993). The seasonal cycle of low stratiform clouds. *Journal of Climate*, *6*(8), 1587–1606. [https://doi.org/10.1175/1520-0442\(1993\)006<1587:TSCOLS>2.0.CO;2](https://doi.org/10.1175/1520-0442(1993)006<1587:TSCOLS>2.0.CO;2)
- Knofczynski, G. T., & Mundfrom, D. (2008). Sample sizes when using multiple linear regression for prediction. *Educational and Psychological Measurement*, *68*(3), 431–442. <https://doi.org/10.1177/0013164407310131>
- Koren, I., Oreopoulos, L., Feingold, G., Remer, L. A., & Altartatz, O. (2008). How small is a small cloud? *Atmospheric Chemistry and Physics*, *8*(14), 3855–3864. <https://doi.org/10.5194/acp-8-3855-2008>
- Kubar, T. L., Waliser, D. E., Li, J. L., & Jiang, X. (2012). On the annual cycle, variability, and correlations of oceanic low-topped clouds with large-scale circulation using Aqua MODIS and ERA-Interim. *Journal of Climate*, *25*(18), 6152–6174. <https://doi.org/10.1175/JCLI-D-11-00478.1>
- López, R. E. (1977). The lognormal distribution and cumulus cloud populations. *Monthly Weather Review*, *105*(7), 865–872. [https://doi.org/10.1175/1520-0493\(1977\)105<0865:TLDACC>2.0.CO;2](https://doi.org/10.1175/1520-0493(1977)105<0865:TLDACC>2.0.CO;2)
- Lovejoy, S. (1982). Area-perimeter relation for rain and cloud areas. *Science*, *216*(4542), 185–187. <https://doi.org/10.1126/science.216.4542.185>
- Medeiros, B., & Stevens, B. (2011). Revealing differences in GCM representations of low clouds. *Climate Dynamics*, *36*(1), 385–399. <https://doi.org/10.1007/s00382-009-0694-5>
- Myers, T. A., & Norris, J. R. (2013). Observational evidence that enhanced subsidence reduces subtropical marine boundary layer cloudiness. *Journal of Climate*, *26*(19), 7507–7524. <https://doi.org/10.1175/JCLI-D-12-00736.1>
- Myers, T. A., & Norris, J. R. (2016). Reducing the uncertainty in subtropical cloud feedback. *Geophysical Research Letters*, *43*, 2144–2148. <https://doi.org/10.1002/2015GL067416>
- Neggers, R. A. J. (2015). Exploring bin-macrophysics models for moist convective transport and clouds. *Journal of Advances in Modeling Earth Systems*, *7*, 2079–2104. <https://doi.org/10.1002/2015MS000502>
- Neggers, R. A. J., Jonker, H. J. J., & Siebesma, A. P. (2003). Size statistics of cumulus cloud populations in large-eddy simulations. *Journal of the Atmospheric Sciences*, *60*(8), 1060–1074. [https://doi.org/10.1175/1520-0469\(2003\)60<1060:SSOCCP>2.0.CO;2](https://doi.org/10.1175/1520-0469(2003)60<1060:SSOCCP>2.0.CO;2)
- Norris, J. R., & Iacobellis, S. F. (2005). North Pacific cloud feedbacks inferred from synoptic-scale dynamic and thermodynamic relationships. *Journal of Climate*, *18*(22), 4862–4878. <https://doi.org/10.1175/JCLI3558.1>
- Nuijens, L., Medeiros, B., Sandu, I., & Ahlgrim, M. (2015). Observed and modeled patterns of covariability between low-level cloudiness and the structure of the trade-wind layer. *Journal of Advances in Modeling Earth Systems*, *7*, 1741–1764. <https://doi.org/10.1002/2015MS000483>

- Nuijens, L., Serikov, I., Hirsch, L., Lonitz, K., & Stevens, B. (2014). The distribution and variability of low-level cloud in the North Atlantic trades. *Quarterly Journal of the Royal Meteorological Society*, *140*(684), 2364–2374. <https://doi.org/10.1002/qj.2307>
- Nuijens, L., & Stevens, B. (2012). The influence of wind speed on shallow marine cumulus convection. *Journal of the Atmospheric Sciences*, *69*(1), 168–184. <https://doi.org/10.1175/JAS-D-11-02.1>
- Nuijens, L., Stevens, B., & Siebesma, A. P. (2009). The environment of precipitating shallow cumulus convection. *Journal of the Atmospheric Sciences*, *66*(7), 1962–1979. <https://doi.org/10.1175/2008JAS2841.1>
- Peters, O., Neelin, J. D., & Nesbitt, S. W. (2009). Mesoscale convective systems and critical clusters. *Journal of the Atmospheric Sciences*, *66*(9), 2913–2924. <https://doi.org/10.1175/2008JAS2761.1>
- Plank, V. G. (1969). The size distribution of cumulus clouds in representative Florida populations. *Journal of Applied Meteorology*, *8*(1), 46–67. [https://doi.org/10.1175/1520-0450\(1969\)008<0046:TSDOCC>2.0.CO;2](https://doi.org/10.1175/1520-0450(1969)008<0046:TSDOCC>2.0.CO;2)
- Qu, X., Hall, A., Klein, S. A., & DeAngelis, A. M. (2015). Positive tropical marine low-cloud cover feedback inferred from cloud-controlling factors. *Geophysical Research Letters*, *42*, 7767–7775. <https://doi.org/10.1002/2015GL065627>
- Rasch, P. J., & Kristjansson, J. E. (1998). A comparison of the CCM3 model climate using diagnosed and predicted condensate parameterizations. *Journal of Climate*, *11*(7), 1587–1614. [https://doi.org/10.1175/1520-0442\(1998\)011<1587:ACOTCM>2.0.CO;2](https://doi.org/10.1175/1520-0442(1998)011<1587:ACOTCM>2.0.CO;2)
- Rieck, M., Nuijens, L., & Stevens, B. (2012). Marine boundary layer cloud feedbacks in a constant relative humidity atmosphere. *Journal of the Atmospheric Sciences*, *69*(8), 2538–2550. <https://doi.org/10.1175/JAS-D-11-0203.1>
- Sakradzija, M., & Hohenegger, C. (2017). What determines the distribution of shallow convective mass flux through a cloud base? *Journal of the Atmospheric Sciences*, *74*(8), 2615–2632. <https://doi.org/10.1175/JAS-D-16-0326.1>
- Sandu, I., & Stevens, B. (2011). On the factors modulating the stratocumulus to cumulus transitions. *Journal of the Atmospheric Sciences*, *68*(9), 1865–1881. <https://doi.org/10.1175/2011JAS3614.1>
- Sengupta, S. K., Welch, R. M., Navar, M. S., Berendes, T. A., & Chen, D. W. (1990). Cumulus cloud field morphology and spatial patterns derived from High Spatial Resolution Landsat Imagery. *Journal of Applied Meteorology*, *29*(12), 1245–1267. [https://doi.org/10.1175/1520-0450\(1990\)029<1245:CCFMAS>2.0.CO;2](https://doi.org/10.1175/1520-0450(1990)029<1245:CCFMAS>2.0.CO;2)
- Slingo, J. M. (1987). The development and verification of a cloud prediction scheme for the ECMWF model. *Quarterly Journal of the Royal Meteorological Society*, *113*(477), 899–927. <https://doi.org/10.1002/qj.49711347710>
- Stein, T. H. M., Holloway, C. E., Tobin, I., & Bony, S. (2017). Observed relationships between cloud vertical structure and convective aggregation over tropical ocean. *Journal of Climate*, *30*(6), 2187–2207. <https://doi.org/10.1175/JCLI-D-16-0125.1>
- Stevens, B. (2005). Atmospheric moist convection atmospheric moist convection. *Annual Review of Earth and Planetary Sciences*, *33*(1), 605–643. <https://doi.org/10.1146/annurev.earth.33.092203.122658>
- Stevens, B., Brogniez, H., Kiemle, C., Lacour, J. L., Crevoisier, C., Kiliani, J., & Stevens, B. (2018). Structure and dynamical influence of water vapor in the lower tropical troposphere. *Shallow Clouds, Water Vapor, Circulation, and Climate Sensitivity* (pp. 199–225). Space Sciences Series of ISSI, vol 65. Springer, Cham. [https://doi.org/10.1007/978-3-319-77273-8\\_10](https://doi.org/10.1007/978-3-319-77273-8_10)
- Tobin, I., Bony, S., Holloway, C. E., Grandpeix, J. Y., Sze, G., Coppin, D., & Roca, R. (2013). Does convective aggregation need to be represented in cumulus parameterizations? *Journal of Advances in Modeling Earth Systems*, *5*, 692–703. <https://doi.org/10.1002/jame.20047>
- Tobin, I., Bony, S., & Roca, R. (2012). Observational evidence for relationships between the degree of aggregation of deep convection, water vapor, surface fluxes, and radiation. *Journal of Climate*, *25*(20), 6885–6904. <https://doi.org/10.1175/JCLI-D-11-00258.1>
- Tompkins, A. M., & Semie, A. G. (2017). Organization of tropical convection in low vertical wind shears: Role of updraft entrainment. *Journal of Advances in Modeling Earth Systems*, *9*, 1046–1068. <https://doi.org/10.1002/2016MS000802>
- van der Dussen, J. J., de Roode, S. R., Dal Gesso, S., & Siebesma, A. P. (2015). An LES model study of the influence of the free tropospheric thermodynamic conditions on the stratocumulus response to a climate perturbation. *Journal of Advances in Modeling Earth Systems*, *7*, 670–691. <https://doi.org/10.1002/2014MS000380>
- Vial, J., Bony, S., Stevens, B., & Vogel, R. (2018). Mechanisms and model diversity of trade-wind shallow cumulus cloud feedbacks: A review. *Shallow Clouds, Water Vapor, Circulation, and Climate Sensitivity* (pp. 159–181), Space Sciences Series of ISSI, vol 65. Springer, Cham. [https://doi.org/10.1007/978-3-319-77273-8\\_8](https://doi.org/10.1007/978-3-319-77273-8_8)
- Weger, R. C., Lee, J., Zhu, T., & Welch, R. M. (1992). Clustering, randomness and regularity in cloud fields: 1. Theoretical considerations. *Journal of Geophysical Research*, *97*(D18), 20,519–20,536. <https://doi.org/10.1029/92JD02038>
- Werner, F., Wind, G., Zhang, Z., Platnick, S., Di Girolamo, L., Zhao, G., & Meyer, K. (2016). Marine boundary layer cloud property retrievals from high-resolution ASTER observations: Case studies and comparison with TerraMODIS. *Atmospheric Measurement Techniques Discussions*, *9*(12), 5869–5894. <https://doi.org/10.5194/amt-2016-265>
- Wielicki, B. A., & Welch, R. M. (1986). Cumulus cloud properties derived using Landsat Satellite Data. *Journal of Climate and Applied Meteorology*, *25*(3), 261–276. [https://doi.org/10.1175/1520-0450\(1986\)025<0261:CCPDUL>2.0.CO;2](https://doi.org/10.1175/1520-0450(1986)025<0261:CCPDUL>2.0.CO;2)
- Wood, R., & Bretherton, C. S. (2006). On the relationship between stratiform low cloud cover and lower-tropospheric stability. *Journal of Climate*, *19*(24), 6425–6432. <https://doi.org/10.1175/JCLI3988.1>
- Yamaguchi, Y., Kahle, A. B., Tsu, H., Kawakami, T., & Pniel, M. (1998). Overview of Advanced Spaceborne Thermal Emission and Reflection Radiometer (ASTER). *IEEE Transactions on Geoscience and Remote Sensing*, *36*(4), 1062–1071. <https://doi.org/10.1109/36.700991>
- Yang, K., Zhang, H., Fu, B., Zheng, G., Guan, W., Shi, A., & Li, D. (2015). Observation of submarine sand waves using ASTER stereo sun glitter imagery. *International Journal of Remote Sensing*, *36*(22), 5576–5592. <https://doi.org/10.1080/01431161.2015.1101652>
- Zhao, G., & Di Girolamo, L. (2007). Statistics on the macrophysical properties of trade wind cumuli over the tropical western Atlantic. *Journal of Geophysical Research*, *112*, D10204. <https://doi.org/10.1029/2006JD007371>